Pontificia Universidad Catolica de Chile
Physics Department

Atomic Force Microscopy study of elastic properties of vapor-phase-deposited lipid membranes

BY

Rodrigo Esteban Catalán López

Thesis presented to the Physics Department of the
Pontificia Universidad Católica de Chile
in partial fulfillment of the requirements for the degree of
Master in Physics.

Supervisor : Dr. Ulrich G. Volkmann (PUC, Chile)
Co-guía : Dr. María José Retamal (PUC, Chile)
Corrector : Dr. Donovan Díaz (PUC, Chile)
Corrector : Dr. Griselda García (PUC, Chile)

May, 2018.

Santiago, Chile.

Acknowledgments

Agradezco al equipo de *Surflab UC* por las herramientas que me han transmitido y que han ayudado a formarme como científico. Doy las gracias, particularmente a mi supervisor, Dr. Ulrich Volkmann, por todo el apoyo y las enseñanzas que me ha brindado durante mi etapa como estudiante de licenciatura y magíster. Agradezco a María Jose Retamal por su apoyo durante el presente trabajo y por haberme instruido en el uso de AFM. A Tomás Corrales por su orientación y por secundarme en la realización de mis propósitos de estudio.

A mis padres, y en general, a mis amigos y familiares más cercanos por la paciencia y el amor que me han dedicado en estos años, demostrado en querer que yo pueda concretar mis sueños, a pesar de que esto implique mi ausencia de muchas de aquellas salidas, almuerzos de fin de semana, y cumpleaños; muchas de aquellas instancias que nos hacen valorar el hecho de *tenernos*.

Finalmente, agradecer a mi esposa por ser un pilar fundamental de apoyo emocional, y por querer acompañarme en este largo y maravilloso camino que he decidido emprender al servicio de la ciencia.

*Este estudio de postgrado fue financiado por Beca Magíster CONICYT-PFCHA/MagísterNacional/2017-22171426.

Contents

1 Introduction **1**

1.1 Biological membranes 3

1.1.1 Phospholipidic structures 4

1.1.1.1 Phase transitions of lipid bilayers 7

1.1.1.2 Phosphatidylcholines 9

1.2 Ellipsometry 10

1.2.1 Light polarization 11

1.2.2 Reflection and transmission of polarized light through plane interfaces 15

1.2.2.1 S-Polarization 16

1.2.2.2 P-Polarization 16

1.2.2.3 Fundamental equation of ellipsometry 16

1.2.3 Drude Theory for ellipsometry 17

1.2.4 Null ellipsometry 19

1.3 Atomic Force Microscopy 20

1.3.1 Principle of operation 20

1.3.2 Detection method 21

1.3.3 Imaging modes of operation of AFM 22

1.3.3.1 Contact Mode 24

1.3.3.2 Intermittent contact or Tapping Mode 24

1.3.3.3 Non-contact mode 25

1.3.4 Force spectroscopy 25

1.3.5 Quantitative Imaging 27

1.3.6 Elasticity measurement 29
1.3.6.1 Young's Modulus 29
1.3.6.2 Hertz model 30
1.3.7 Calibration of the cantilever 32
1.3.7.1 Thermal noise calibration 32
1.3.7.2 Contact-based calibration 33
1.3.7.3 Sader calibration 33
1.4 Raman spectroscopy 34

2 Experimental Procedures **36**
2.1 Sample Fabrication 36
2.1.1 Cleaning process 36
2.1.2 Physical vapor deposition of the phospholipids 37
2.1.2.1 Evaporation chamber setup 37
2.1.2.2 VHRE-controlled evaporation procedure 38
2.2 Characterization 40
2.2.1 Raman spectroscopy 40
2.2.2 Atomic Force Microscope 40
2.2.2.1 General setup 40
2.2.2.2 Adjustment of the detection system 42
2.2.2.3 Calibration of the cantilever 43
2.2.2.4 Data obtention using QI 43
2.2.2.5 Data processing 44

3 Results and discussion **46**
3.1 Raman spectroscopy 46
3.2 Breakthrough force 47
3.3 AFM topography 48
3.4 Young's modulus histogram 50
3.5 Elastic modulus vs temperature 54

4 Conclusions and future work **58**

Abstract

In this work we present a study of phase transitions and their relation with the elastic properties of three phospholipid membranes, namely 1,2-dimyristoyl-sn-glycero-3-phosphocholine (DMPC), 1,2-dipalmitoyl-sn-glycero-3-phosphocholine (DPPC) and 1,2-distearoyl-sn-glycero-3-phosphocholine (DSPC). Samples were generated individually by physical-vapor-deposition of the lipid molecules mentioned over acid-cleaned polished silicon chips. The thickness of the samples were measured with Very High Resolution Ellipsometry. Average thickness are 60Å thickness on average. The molecular consistency of the lipids were characterized using Raman spectroscopy. The Young's modulus of the lipid membranes was obtained applying the Hertz model to data acquired with Atomic Force Microscopy in Quantitative Imaging feedback mode. Finally, the individual dependence of these lipids respect to temperature changes was used to detect the main gel-to-fluid phase transition.

The results in the present work show an expected softening of the lipid membranes just after the main phase transition, although the values of the elastic modulus found do not match the ones reported in the literature. However, the general trends correlate well with the ones found in other works. Nevertheless, systematic investigations using similar conditions as ours are still scarce.

The acquisition of information related to the elastic properties and stability of the membranes is relevant for future works on protein insertion, and to understand the lipid membranes dependance on several other environmental conditions like changes in temperature, pH-dependence or ionic strength concentration.

Chapter 1

Introduction

During the last decades, studies concerning the assembly of artificial membranes over solid substrates have taken center stage due to the potential applications in the fields of bionanotechnology and fabrication of biosensors. Of special importance are studies about lipid membranes, which surround the living cells and play several functions in conjunction with proteins such as controlling the exchange of nutrients from the interior to the exterior of the cells and vice versa, and allow the transition of electric signals that establish the intercommunication among cells.

Supported lipid membranes provide a model system for investigating the properties and functions of the cell membrane [1]. Several techniques have been employed to quantitatively investigate a variety of properties of lipid bilayer, such as electron microscopy or scanning differential calorimetry (SDC). An important technique that provides quantitative information about the mechanical properties of the membranes is the micropipette aspiration technique, which has been reported for measuring elastic moduli for area dilation, shear and bending [2].

The type of experiments that study phospholipidic membranes, while crucial, are mostly restricted to the use of giant vesicles, providing a *mesoscopic* outlook on bilayer mechanical stability. However, the chemical diversity of the cell membrane demands experimental techniques able to probe the local elastic properties with nanometer resolution [3]. At this scale, the mechanical characterization of

lipid membranes is best probed when they are supported onto solid substrates. According to this approach, Atomic Force Microscopy (AFM), has emerged as an indispensable tool to gain insights into the topology of lipid membranes, allowing measurements of the nanomechanical properties using force spectroscopy mode, operating under constant velocity [4]. Contrary to using vesicles, the solid supports constrain the lipid membranes to nearly planar geometry[5], such that they can only be compressed in the vertical direction [6]. Much of the literature about studies of mechanical properties of phospholipidic membranes recurs to time-consuming methods, such as single force-distance curves. However, new AFM techniques have been developed or enhanced since the invention of a pulsed-force mode in 1997, being *Quantitative Imaging* mode the most prominent nowadays for measuring elastic properties of thin films.

The present work aims to study the nanomechanical properties of planar phospholipid membranes DMPC, DPPC, and DSPC individually, which have been deposited onto silicon substrates from their gas phase. The study involves using the novel *Quantitative Imaging* (QI) AFM mode which will give us insights into the change of the elastic Young's modulus of these membranes under temperature-controlled settings in water environment. If the changes in the elastic modulus occur at or near the reported phase transition temperatures of lipid bilayers, then we can be sure that our artificial lipid bilayers have formed and that our method for bilayer formation is successful. Unlike x-ray methods or differential scanning calorimetry, AFM in QI-mode is a *direct* method for study of the mechanical properties of supported lipid membranes. In other words, AFM is an additional powerful tool for the detection of phase transition temperatures in artificial membranes. Special importance is given to the phase transition of lipid membranes due to their biological relevance. In fact, several membrane functions, such as ion permeability or lateral diffusion, can differ significantly in various phases.

1.1 Biological membranes

One of the most important characteristics of the structure of cells is the separation between internal structures of the cytoplasm and the external environment. In eukaryotic cells, furthermore, there are also cytoplasmic compartments present, in which certain cellular activities can be separated in order to increase the efficiency of the cell's processes. This separations are achieved by a wall of both complex organic and functional molecules, namely phospholipids and proteins, respectively. As this natural barrier is composed mainly by phospholipids, it has been given the name *phospholipidic membrane*.

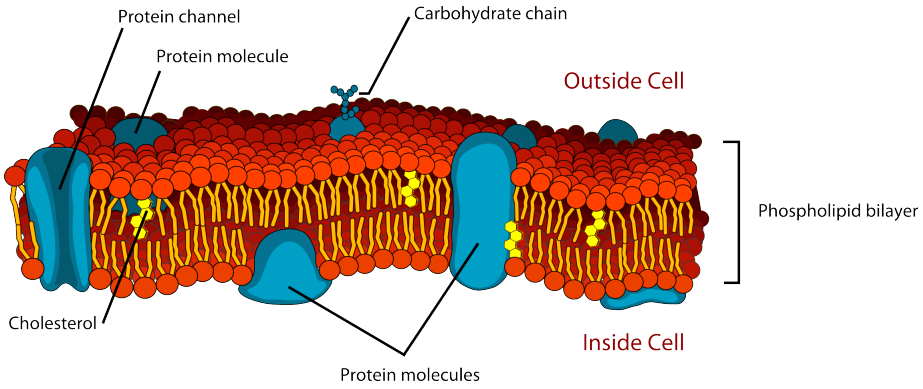

Figure 1.1.1: *Representation of a phospholipid bilayer. Its major components are phospholipids, as well as peripheral and transmembrane proteins which regulates the cell's functional processes (figure adapted from [7]).*

According to the fluid mosaic model devised by Singer and Nicolson [8], all cell membranes exhibit a plethora of membrane spanning proteins that are embedded in the phospholipidic membranes and can interact with the surrounding phospholipids, as seen from several examples. On the one hand, changes in the phospholipid environment of these biological layers can regulate or alter the functions, for instance, of intrinsic membrane proteins. On the other hand, peripheral (or *extrinsic*) proteins, can influence and be influenced by lipid structure and composition in the membrane [9]. Thus, it is seen that lipid-protein interactions play important roles in both directions. In addition, some studies show that lipid membrane modifications regulate three important cell processes, such as the

structure of the phospholipids, the formation of lipid domains and clustering of G-protein peptides [10, 11].

As most of the cell's functions occur in or around these membranes, they are of high interest for researchers for the development of future medical and biological nano-devices.

1.1.1 Phospholipidic structures

Lipids are organic molecules which are mainly composed of carbon and hydrogen, and to a lesser extent of oxygen and other elements such as sulfur and phosphorus. They are found as natural molecules in fats, waxes, triglycerides and phospholipids, among other molecules. Some lipids are characterized for being hydrophobic, which makes them non-soluble in water. Other types, known as *amphiphilic* or *amphipathic* lipids, are of profound interest because those molecules exhibit specific *zones* which can have affinity to water molecules, thus named *hydrophilic*, and other zones that reject water molecules, named *hydrophobic*. This remarkable feature allows this lipids to form interesting structures when they are exposed to a water ambient. Phospholipids are, maybe, the most known example of these kinds of molecules.

Phospholipids are a class of lipids which constitute the main components of biological membranes. They highlight two hydrophobic structures identified as *tails*, consisting of chains of fatty acids. They also exhibit an hydrophilic array of atoms, a structure known as *head* (sometimes addressed as *polar head group*), which contains a phosphate group. Both structures are held together by a molecule of glycerol, as seen in the following image:

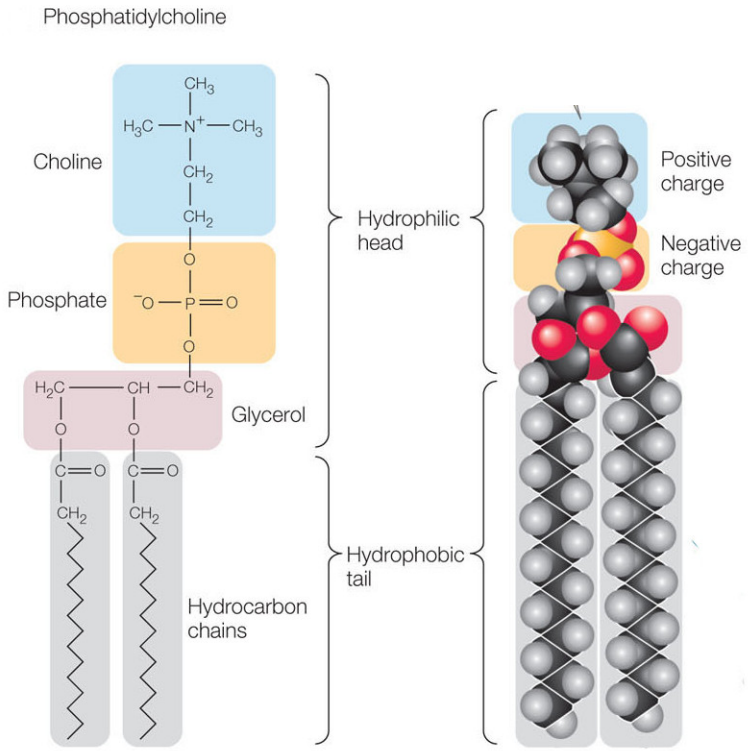

Figure 1.1.2: *Representation of a phospholipid molecule. The very distinctive structural property of this molecules are the hydrophilic polar 'head' group and the hydrophobic hydrocarbon 'tails' (figure adapted from [12])*

The structural and physical properties of phospholipids have two remarkable consequences as they are exposed to a water environment. First, polar head groups interact with water molecules, whereas the hydrocarbon chains tend to avoid the interaction with them. Second, due to their amphiphilic nature, a spontaneously-emergence of ordered-like phospholipid structures can take place under certain concentrations. Micelles are the simplest type of construction formed by the association of amphiphiles. They consist of a core of hydrophobic interacting alkyl chains shielded from contact with water molecules by hydrophilic polar heads groups (see Fig. 1.1.3). The formation of this structures occurs above the so called *critical micellar concentration* (CMC). The formation of micelles results from both enthalpic and (mostly) entropic contributions.

Enthalpy contribution comes from the energetically favorable enhancement of interactions between hydrocarbon chains. Entropic contribution arises from a favoring structuration of water molecules. Unassociated hydrocarbon chains in bulk water break up the hydrogen bonds between H_2O molecules and impose a locally more ordered configuration that is entropically unfavorable. When micelles are formed, however, the disruption of water structure is reduced, therefore they are entropically favored compared to unasocciated phospholipid molecules [13].

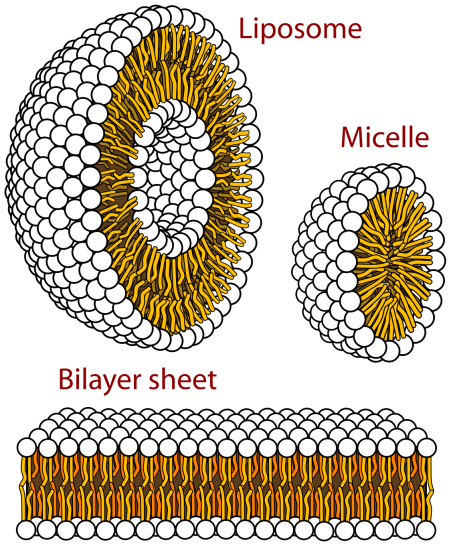

Figure 1.1.3: *Structures formed by amphiphilic molecules in aqueous medium. White dots represent hydrophilic polar head groups, whereas yellow stripes represent hydrophobic chains of hydrocarbon (figure adapted from [7]).*

Increasing the concentration of amphiphilic molecules in the solution can lead to lamellar structures, in which the hydrophobic tails are facing to each other and the hydrophilic heads form the inner and outer core of the structure, forming a bilayer (see Fig. 1.1.3) . The most important example of lamellar structure are vesicles or liposomes. Vesicles are hollow aggregates made from one or more amphiphilic bilayers. Vesicles formed from a single bilayer are called unilamellar, while the ones formed by more than one bilayer are called multilamellar. Vesicles can be formed not only depending on the concentration of phospholipids in

aqueous solution but also on the type of amphiphile. For instance, double chain lipids often form lamellar phases directly upon increasing concentration at the CMC, whereas single-chained lipids tend to form micelles. The forces holding these structures are weak van der Waals, hydrophobic, hydrogen-bonding and electrostatic interactions. The weak nature of these forces makes the structures flexible.

In case that bilayers are assembled over wet planar substrates they are named supported lipid bilayers (SLB) or supported planar lipid bilayers (SPLB). One of the main reasons for the study of artificial membranes as SLBs is that the substrate allows for stability of these layers [14], which is something difficult to control using vesicles due to their fragility and instability over longer periods of time. SLB membranes have attracted much attention since they can also provide a model system for investigating the properties and functions of the cell membrane. Therefore, in this work we are going to be concerned to the study of the mechanical properties of SLBs.

1.1.1.1 Phase transitions of lipid bilayers

Phospholipidic membranes exhibit distinct phase transitions, associated typically with changes in temperature. The phase behavior of phospholipids in water systems are of interest in several disciplines because of the possible biological relevance of the different phases that they form and the transitions that they undergo. Each phase features a change in the hydrophobic tails of the lipid molecules as shown by experiments that have identified a number of arrangements of lipid bilayers. All SLBs can exist in several known phases such as crystalline, gel or liquid. In addition, a number of intermediate stable, metastable, and transient lamellar gel structured are adopted by different lipids [15]. The distinct phases are shown in the following image:

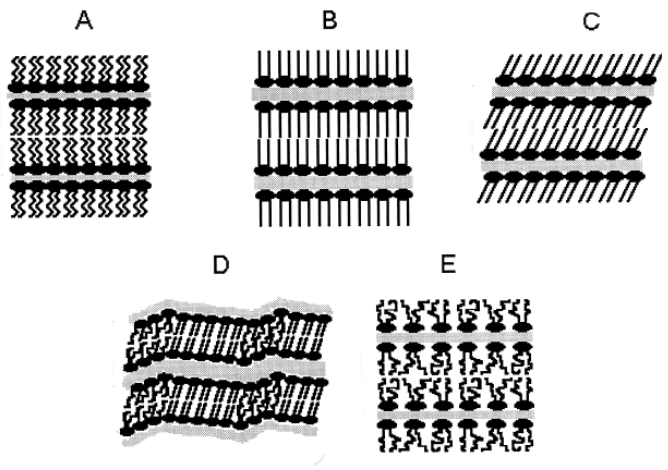

Figure 1.1.4: *Schematic of several lamellar phases in hydrated lipid bilayers: (A) Subgel L_c; (B) gel (untilted chains) L_β; (C) gel (tilted chains) $L_{\beta'}$; (D) rippled gel $P_{\beta'}$; (E) liquid crystalline L_α (Adapted from* [16]*).*

To identify the phase transitions of lipid bilayers a combination of uppercase latin letters and lowercase greek letters is used. Latin letters represent long-range order (i.e. lamellar L, rippled P, for instance) and greek letters stand for short-range order (α for disordered and melted, β for semi-ordered elongated chains). The most important phases are as follows:

- L_c known as lamellar crystalline phase exhibits the carbon chains straight (see Fig 1.1.4, A).
- L_β is a lamellar gel phase in which the carbon chains are elongated and straight (see Fig 1.1.4, B).
- $L_{\beta'}$ is a lamellar gel phase in which the carbon chains are elongated and tilted (see Fig 1.1.4, C).
- $P_{\beta'}$ is a ripple gel phase in which the bilayer is wavy and the carbon chains are elongated and straight (see Fig 1.1.4, D).
- L_α is a lamellar fluid phase in which the carbon chains are melted (see Fig 1.1.4, E).

The phase behavior is dominated by the main gel-fluid phase transition $L_\beta \rightarrow L_\alpha$ associated with the melting of the lipid hydrocarbon chains. This transition

highlights the change from ordered to disordered arrangements of chains [17]. A temperature is associated to each phase transition in a lipid bilayer but the one that matters the most is the one accounting for the main phase transition T_m.

1.1.1.2 Phosphatidylcholines

Phosphatidylcholines (PCs) represent the most abundant lipid class in mammalian membranes and a major membrane component in eukaryotic organisms. In addition, this sort of molecules are also critical constituents of human lung surfactant, serum lipoproteins, and bile, representing the most widely used lipid model in artificial biological membrane studies [16].

Dipalmithoylphosphatidylcholine or DPPC is perhaps the most studied exemplar of phospholipids as it is the principal component of the pulmonary surfactant and the most preferred liposome for the study of model biological membranes [18, 19, 20]. Its structure consists of a hydrophilic polar *head* which is composed by a nitrogen group with positive charge, and a phosphate group with negative charge. In addition, a pair of aliphatic chains consisting of 16 carbon atoms conform the hydrophobic tails of this phospholipid. The approximate length of this molecules is about 2,5 nm [21] which would result in an approximate 5 nm phospholipid bilayer.

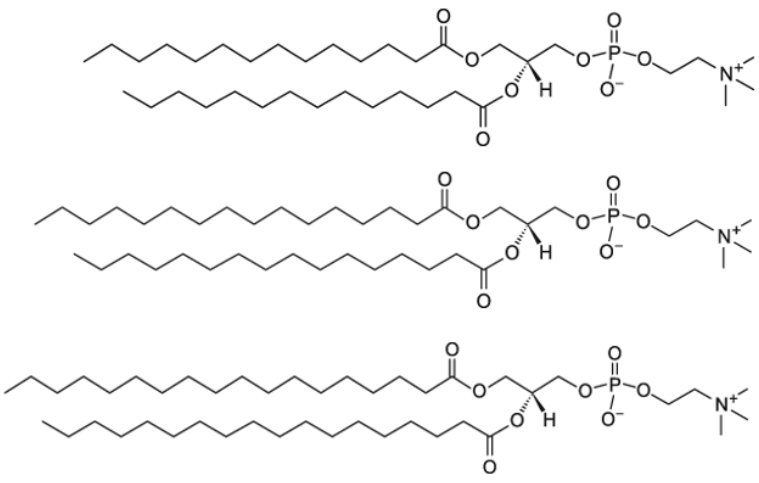

Figure 1.1.5: *Phosphatidylcholine molecules. From top to bottom: DMPC, DPPC and DSPC (adapted from [22]).*

Similar molecules, such as dimyristoylglycerophosphocholine (DMPC) and distearoylglycerophosphocholine (DSPC) are also used as model SLBs and will be also used in the present work. As seen in Figure 1.5 DMPC, DPPC, and DSPC have almost the same molecular structures differing only in the number of carbon atoms in their hydrophobic tails. DMPC exhibits the shortest carbon tail formed by 14 carbon atoms, whereas DPPC and DSPC have 16 and 18 carbon atoms respectively.

Carbon chain length influences on the value of the main transition temperature T_m. The longer the carbon chains the higher the gel-to-fluid temperature due to an increasing interaction among the chains and other phospholipids. In fact, DMPC melting transition is reported to be 23^{o}C - 24^{o}C [23], DPPC has a melting point in 41^{o}C - 42^{o}C [24], and DSPC in 54^{o}C - 55^{o}C [25]. These temperatures usually are given in wider ranges because phase transition depends on the ambient conditions such as pH, ionic strength, or substrate to which the PCs are exposed to.

1.2 Ellipsometry

Ellipsometry is an experimental technique which measures changes in the state of polarization of a laser beam which is reflected from the surface of a certain material. The information obtained from the measurements depends on the optical properties as well as on the thickness of the materials. In consequence, ellipsometry is used mainly to assess the thickness of thin films and their optical constants. In addition, its application can be widely extended to characterize sample composition, crystallinity, roughness, among other properties associated to a change in their optical response. A great advantage of this technique is that it is non-destructive, which allows for the conservation of properties of the samples studied. The following section describes the ellipsometric theory and operation of a *very high resolution ellipsometer* (VHRE), which will be mainly

used to measure the thickness of a thin layer of phospholipid deposited onto a silicon substrate.

1.2.1 Light polarization

Polarization is a fundamental property of light, which has been studied to a large extent since its discovery made by the french physicist Étienne-Louis Malus in 1808. The interaction of light with matter is related to the induced motion of electric charges from electrons and atomic nuclei. A detailed description of light is achieved using vectors representing plane-perpendicularly-oscillating electric and magnetic fields, which are both also perpendicular to a propagation vector. It is possible to underestimate the magnetic induction in a medium where light strikes on, because changes in the magnetic moment vectors are quite slow to follow the fast oscillations of the magnetic and electric fields [26]. Under this consideration, the most important physical quantity to describe the properties of light will be the electric field vector $\vec{E}$. The existence of preferred directions established in the interaction between the electric field of an electromagnetic wave with the electric charges in matter gives importance to the study of the phenomenon of *polarization*.

Polarization is understood as the trajectory described by the electric field vector of an electromagnetic wave. It is said that light is *polarized* when there is a preferred trajectory outlined by the electric field vector at the moment it changes its amplitude over time. There are three states of polarization of light:

1. Linear polarization: It is produced when the components x and y of the electric field vector are in phase.

2. Circular polarization: It is produced when the electric field components have the same amplitude and they are out of phase by 90^{o}, either forward or backwards. This sets whether the electric field vector moves clockwise or counterclockwise.

3. Elliptic polarization: In this case, the amplitudes of the components of the

electric field vector within the plane of propagation are not equal, and there is also a phase shift between 0^{o} and 360 ^{o}.

This last sort of polarization is the most probable to occur, leaving linear and circular polarization as particular cases.

Considering a monochromatic wave propagating in the z direction, one would have the following figure that illustrates the three types of polarization:

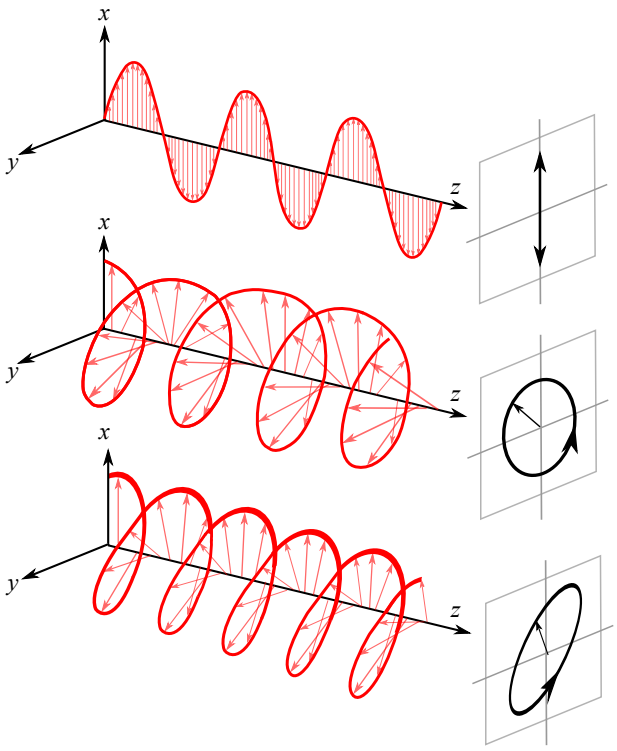

Figure 1.2.1: *Fundamental states of polarization of an electromagnetic wave (Adapted from [27]).*

If a monochromatic wave strikes a reflecting surface, it defines a plane of incidence which is perpendicular to the surface and contains the wave vector $\vec{k}_{in}$. The electric field vector $\vec{E}$ and the magnetic field vector $\vec{B}$ are perpendicular to each other and also to the wave vector. It is possible to represent the electric field using two components oscillating in the plane of propagation: π / parallel and σ / perpendicular, as seen in the following illustration:

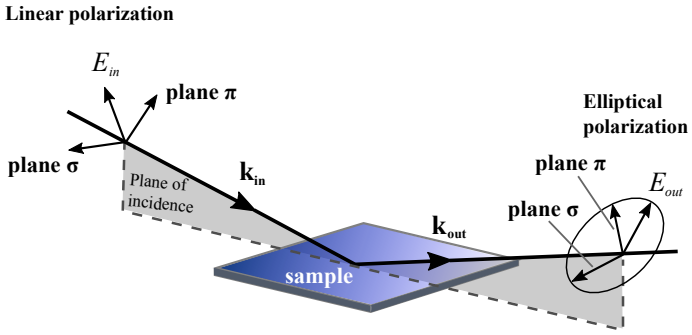

Figure 1.2.2: *Trajectory of an incident light beam over a reflecting substrate. The plane of incidence contains the incident beam and the reflected beam (Adapted from [27]).*

Spatial and time dependence of the electric field vector $\vec{E}(\vec{r},t)$ in a uniform and isotropic medium of constant permitivity ε can be described by the wave equation:

$$\left[\nabla^2 - \frac{\varepsilon(\omega)}{c^2}\frac{\partial^2}{\partial t^2}\right]\vec{E}(\vec{r},t) = 0 \tag{1.1}$$

where ω is the angular frequency of the wave, and c is the speed of light in vacuum. One solution to the wave equation corresponds to a monochromatic wave propagating along the z-axis in an orthogonal coordinate system:

$$\vec{E}(z,t) = Re\left\{\begin{bmatrix}E_x\\E_y\end{bmatrix}e^{i(k_z z-\omega t+\delta)}\right\} \tag{1.2}$$

where:

$$E_x(z,t) = A_x\cos(k_z z-\omega t+\delta_x) \tag{1.3}$$

$$E_y(z,t) = A_y\cos(k_y z-\omega t+\delta_y) \tag{1.4}$$

One can discard the spatial and temporal dependence because one is mainly interested in the state of polarization, obtaining:

$$\vec{E} = \begin{bmatrix}E_x\\E_y\end{bmatrix} = \begin{bmatrix}A_x e^{i\delta_x}\\A_y e^{i\delta_y}\end{bmatrix} \tag{1.5}$$

The condition for elliptic polarization means that the component of the $\vec{E}$ vector must satisfy the constraint equation:

$$\frac{E_x^2}{A_x^2} + \frac{E_y^2}{A_y^2} = 1 \tag{1.6}$$

One can introduce the expression $\chi = E_x/E_y$, and define E_i and E_o as the incident and outward components of the electric field vector, which gives:

$$\frac{\chi_i}{\chi_o} = \frac{E_{iy}E_{ox}}{E_{ix}E_{oy}} \tag{1.7}$$

By the definition of the electric field vector:

$$\frac{\chi_i}{\chi_o} = \frac{A_{iy}e^{i\delta_{iy}}E_{ox}e^{i\delta_{ox}}}{A_{ix}e^{i\delta_{ix}}E_{oy}e^{i\delta_{oy}}} = \frac{A_{iy}}{A_{ix}}e^{i\left(\delta_{iy}-\delta_{ix}\right)}\frac{A_{ox}}{A_{oy}}e^{i\left(\delta_{ox}-\delta_{oy}\right)} \tag{1.8}$$

Considering the incident wave as a linearly polarized wave, then $\delta_i = 0$ and $A_{ix} = A_{iy}$. Thus:

$$\frac{\chi_i}{\chi_o} = \frac{A_{ox}}{A_{oy}}e^{i\left(\delta_{ox}-\delta_{oy}\right)} \tag{1.9}$$

Looking at these parameters in an ellipse like the one shown below:

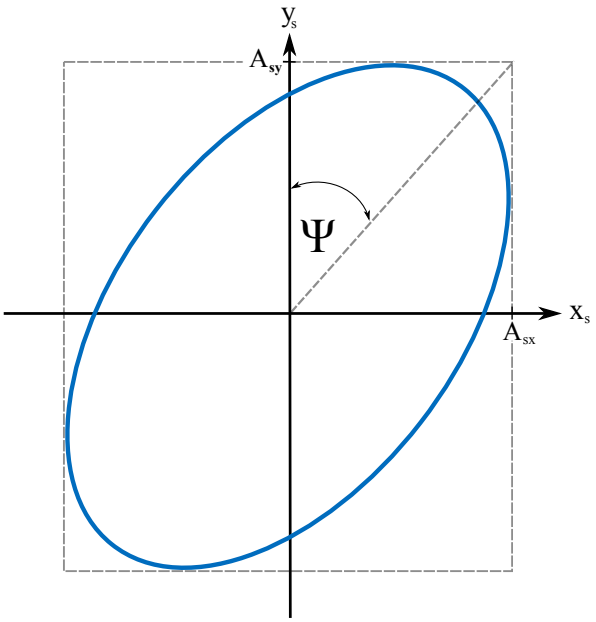

Figure 1.2.3: *Projection of an elliptically polarized wave on a plane (Adapted from [27]).*

one can observe that:

$$\tan\Psi = \frac{A_{ox}}{A_{oy}} \tag{1.10}$$

$$\Delta = \delta_{ox} - \delta_{oy} \tag{1.11}$$

thus:

$$\frac{\chi_i}{\chi_o} = \tan\Psi e^{i\Delta} \tag{1.12}$$

1.2.2 Reflection and transmission of polarized light through plane interfaces

At the moment of studying reflection and transmittance of a polarized electromagnetic wave over plane substrates, one considers a monochromatic wave propagating in the plane $x-z$, striking on a plane interface between two semi-infinite medium of different refractive index, as shown in the following picture.

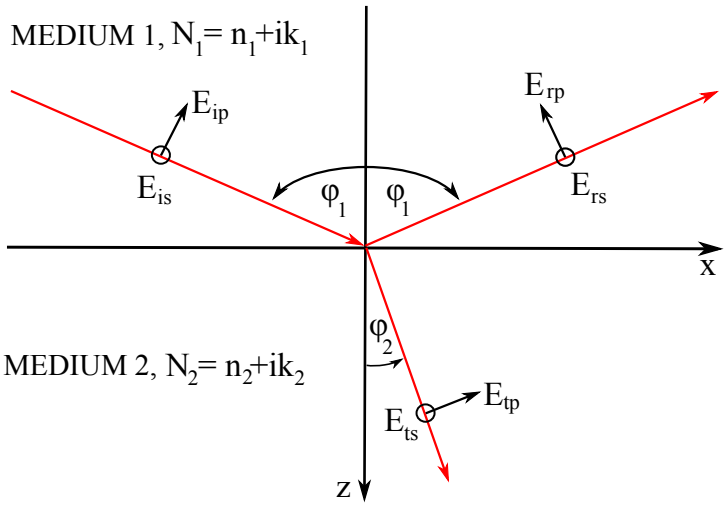

Figure 1.2.4: *Reflection and transmission of a plane electromagnetic wave on a plane interface. Both incident and reflected beam define a plane of incidence (Adapted from [26]).*

The state of polarization that gets the reflected beam and the one transmitted depends on the polarization and the direction of oscillation of the electric field vector of the incident wave. Two cases can be distinguished for monochromatic

plane waves with linear polarization.

1.2.2.1 S-Polarization

For an incident wave with linear polarization and perpendicular to the plane of incident, according to Figure 1.2.4 one can denote E_{is}, E_{rs}, y E_{ts} as the amplitudes of the incident waves, reflected and transmitted, respectively. One can express the Fresnel coefficients, obtaining:

$$r_s \equiv \frac{E_{rs}}{E_{is}} = \frac{N_1 \cos\varphi_1 - N_2 \cos\varphi_2}{N_1 \cos\varphi_1 + N_2 \cos\varphi_2} \tag{1.13}$$

$$t_s \equiv \frac{E_{ts}}{E_{is}} = \frac{2N_1 \cos\varphi_1}{N_1 \cos\varphi_1 + N_2 \cos\varphi_2} \tag{1.14}$$

1.2.2.2 P-Polarization

For an incident wave with linear polarization parallel to the plane of incidence one can denote, again noting Figure 1.2.4, E_{ip}, E_{rp} y E_{tp} as the amplitude of the incident, reflected and transmitted wave, respectively. The Fresnel coefficients in this case are:

$$r_s \equiv \frac{E_{rp}}{E_{ip}} = \frac{N_1 \cos\varphi_2 - N_2 \cos\varphi_1}{N_1 \cos\varphi_2 + N_2 \cos\varphi_1} \tag{1.15}$$

$$t_s \equiv \frac{E_{ts}}{E_{is}} = \frac{2N_1 \cos\varphi_2}{N_1 \cos\varphi_2 + N_2 \cos\varphi_1} \tag{1.16}$$

1.2.2.3 Fundamental equation of ellipsometry

Considering the Snell equations, it is possible to write the reflection coefficient for both S and P polarizations as follows:

$$r_s = \frac{\sin(\varphi_2 - \varphi_1)}{\sin(\varphi_2 + \varphi_1)} = \frac{N_1 \cos\varphi_1 - \sqrt{N_2^2 - N_1^2 \sin^2\varphi_1}}{N_1 \cos\varphi_1 + \sqrt{N_2^2 - N_1^2 \sin^2\varphi_1}} \tag{1.17}$$

$$r_p = \frac{\tan(\varphi_2 - \varphi_1)}{\tan(\varphi_2 + \varphi_1)} = \frac{N_1/\cos\varphi_1 - N_2/\sqrt{1 - \left(\frac{N_1}{N_2}\right)^2 \sin^2\varphi_1}}{N_1/\cos\varphi_1 + N_2/\sqrt{1 - \left(\frac{N_1}{N_2}\right)^2 \sin^2\varphi_1}} \tag{1.18}$$

One can write the reflection coefficients as:

$$r_s \equiv \tan\psi_s e^{i\Delta_s} \tag{1.19}$$

$$r_p \equiv \tan\psi_p e^{i\Delta_p} \tag{1.20}$$

Defining ρ as the ratio between the Fresnel coefficients for reflection, it is possible to obtain the fundamental equation of ellipsometry [26]:

$$\rho \equiv \frac{r_p}{r_s} = \frac{\tan\psi_s}{\tan\psi_p} e^{i\left(\Delta_p - \Delta_s\right)} = \tan\Psi e^{i\Delta} \tag{1.21}$$

The importance of this equation falls on the parameters Ψ and Δ that can be related with the thickness or the refraction index for thin films [28].

1.2.3 Drude Theory for ellipsometry

In the previous sections, Fresnel equations for S and P polarizations of reflected and transmitted waves in a flat interface were presented. It is possible to consider a system composed by *ambient-thin film-silicon*, that is, two interfaces, on which it is possible to apply the Fresnel equations.

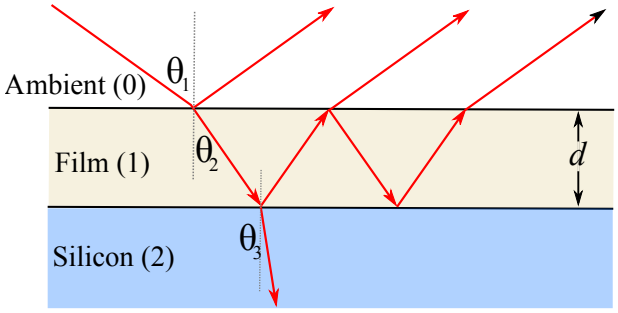

Figure 1.2.5: *Reflected and refracted beams in each layer generate multiple beams in a thin film. The interference with one another depends on the relative phase and amplitudes of the electric field.*

As the reflected rays have reflection and transmission components of the film, the total amplitude of the reflected beam will be the sum of each of the output amplitudes:

$$R = r_{01} + t_{01}t_{10}r_{12}e^{-2i\beta} + t_{01}t_{10}r_{10}r_{12}^{2}e^{-4i\beta} + t_{01}t_{10}r_{10}^{2}r_{12}^{3}e^{-6i\beta} + \cdots \tag{1.22}$$

in which one considers:

$$\beta = 4\pi\frac{d}{\lambda}\sqrt{N_1^2 - N_0^2\sin^2\theta_1} \tag{1.23}$$

It is possible to see that R corresponds to a geometric sequence, which can be simplify as to:

$$R = r_{01} + \frac{t_{01}+t_{10}e^{-2i\beta}}{1+r_{01}r_{12}e^{-2i\beta}} = \frac{r_{01}+r_{12}e^{-2i\beta}}{1+r_{01}r_{12}e^{-2i\beta}} \tag{1.24}$$

In this manner:

$$R_p = \frac{r_{01p}+r_{12p}e^{-2i\beta}}{1+r_{01p}r_{12p}e^{-2i\beta}} \tag{1.25}$$

$$R_s = \frac{r_{01s}+r_{12s}e^{-2i\beta}}{1+r_{01s}r_{12s}e^{-2i\beta}} \tag{1.26}$$

This values can be inserted into the equation (1.21), from which it is possible

to obtain:

$$\rho = \frac{\left(r_{01p} + r_{12p}e^{-2i\beta}\right)\left(1 + r_{01s}r_{12s}e^{-2i\beta}\right)}{\left(1 + r_{01p}r_{12p}e^{-2i\beta}\right)\left(r_{01s} + r_{12s}e^{-2i\beta}\right)} \tag{1.27}$$

Putting appropriate terms together and using the Fresnel coefficient it is possible to obtain the fundamental equation of ellipsometry:

$$\rho = \tan\Psi e^{i\Delta} \tag{1.28}$$

in which:

$$\Psi \equiv A \tag{1.29}$$

$$\Delta \equiv 2P + \frac{\pi}{2} \tag{1.30}$$

being P and A the polarization angles measured by a polarizer and an analyzer, respectively [29, 30].

1.2.4 Null ellipsometry

One of the most important techniques applied in ellipsometry is known as *null ellipsometry*. This procedure uses a PCSA optical system (*Polarizer-Compensator-Sample-Analyzer*), as shown in the following image:

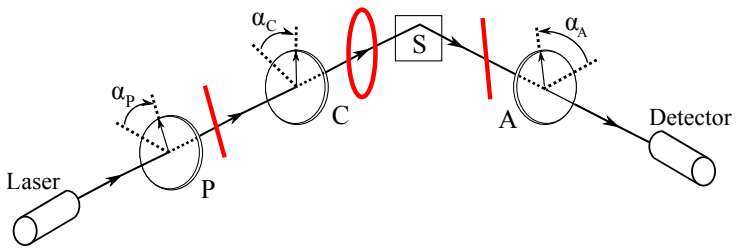

Figure 1.2.6: *PCSA configuration for null ellipsometry. The picture shows changes in the state of polarization of the laser beam (Adapted from [26]).*

The polarizer P is used to select a certain linear state of polarization. The compensator C retards the phase of the wave passing through it in order to

produce an elliptically polarized wave, which ultimately strikes upon the sample S and it is reflected away from it. The ellipticity of the given state of polarization is picked, so as to make it the opposite to the state of polarization of the beam reflected off the sample. Thus, the final polarization of the reflected beam is linear and its intensity can be brought to a minimum using an analyzer A.

1.3 Atomic Force Microscopy

The atomic force microscope (AFM) stands as one of the most versatile members of a family of microscopes known as scanning probes microscopes (SPMs). These instruments generate images by *sensing* rather than *looking* at specimens. The SPMs began in the early 1980s when Binning and Rohrer revolutionized microscopy through the invention of the scanning tunneling microscope (STM) [31]. A few years later, Binning et. al., in 1986, announced the birth of the second member of the SPM family, the atomic force microscope [32], which did not appear commercially until the early 1990s and have been improved ever since.

1.3.1 Principle of operation

The way an AFM operates is easy to understand. However, when one thinks about a *microscope*, in the case of the AFM, one must discard all previous notions of conventional microscopy since AFMs have no lenses of any kind. In fact, the imaging technique is achieved by a mechanical device, namely the *cantilever*, which is a probe with a sharp tip, as shown in Fig. 1.3.1 able to sense very small forces when atoms or molecules come closer. The cantilevers are flexible devices, which can be modeled as springs that measure the force between the tip of the cantilever and the sample. The idea is that repulsive or attractive forces between the tip and the sample is converted into a deflection of the cantilever. The cantilever is attached to a rigid substrate that can be held fixed, and depending on whether the interaction is repulsive or attractive, the cantilever bends away or towards the sample.

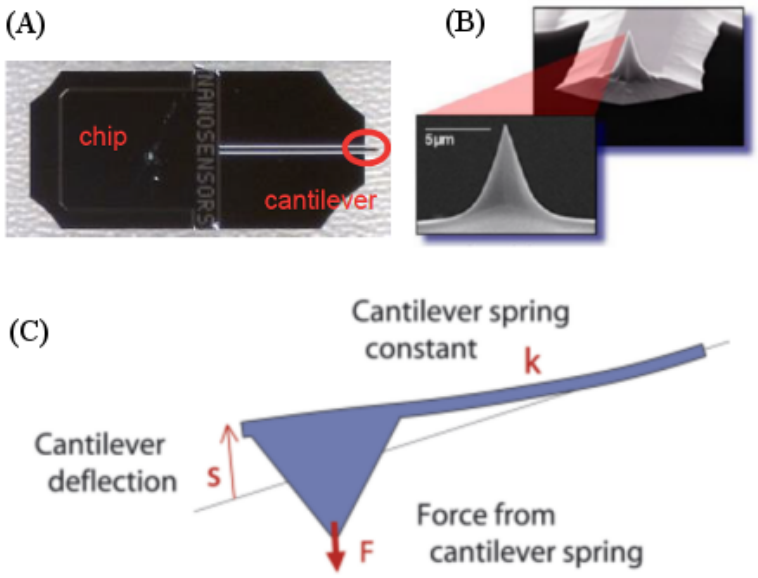

Figure 1.3.1: *(A) The chip the cantilever is attached to is shown; (B) SEM image of the tip of the cantilever. The tip length is usually a few microns; (C) Scheme of a cantilever of spring constant k increases with lever thickness but decreases with cantilever length (Adapted from [33]).*

Irrespective of the geometry, the force contribution F from the bending of the cantilever is determined by the simple equation that dictates Hooke's Law:

$$F = -ks \tag{1.31}$$

where k is the spring constant of the cantilever and s is its displacement. The minus sign indicates that the force acts in the opposite direction to the displacement of the cantilever. The spring constant k increases with lever thickness but decreases with cantilever length.

1.3.2 Detection method

Although there are several methods to detect the deflection of a cantilever, they can be catalogued into two categories: optical and electrical detectors. The detection method that concern us in this work is an optical method in which a four-quadrant photodetector is used. This has become the standard method for

most of the AFMs and depicts a laser beam that is reflected from the back of the cantilever onto the photodetector, as shown in the following image:

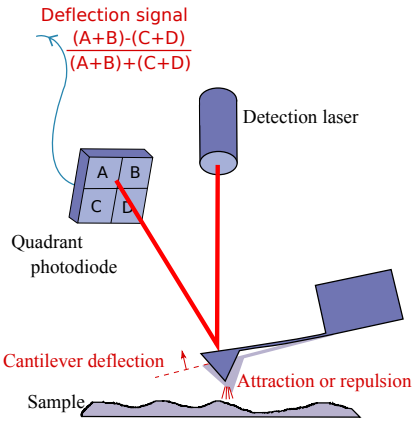

Figure 1.3.2: *Schematic image about the detection system of AFM. As the tip scans over the sample the cantilever is deflected causing a displacement of the laser spot on the photodiode (Adapted from [33]).*

Most AFMs use a photodiode that is composed of four quadrants. This allows the laser spot position to be calculated in two directions: vertical and lateral. The vertical deflection accounts for the measurement of the interaction force and can be calculated by comparing the amount of signal from the *top* and *bottom* halves of the detector. The lateral displacement of the laser beam accounts for the twisting of the cantilever and can be calculated by comparing the *left* and *right* halves of the detector. This simple system is surprisingly sensitive enough to detect atomic scale movement of the tip as it traverses the sample. The information acquired by the quadrant photodiode is converted into an electrical signal which is sent to a feedback control that keeps an appropriate scanning of the tip along the sample. An appropriate adjustment of the feedback control is crucial to obtain a good image. There are several modes of operation of the feedback control in the AFM which are outlined next.

1.3.3 Imaging modes of operation of AFM

Data acquisition for image generation involves the interaction of long and short range forces between the tip and the sample. The longer-range attractive forces

are usually van der Waals forces and capillary forces, and the repulsive interaction takes over at short ranges as the electron orbitals of the atoms in the tip start to overlap with the ones of the sample. Nearly all AFM techniques employ a feedback loop to hold a constant interaction between the tip and the sample as the tip scans the surface. This system detects the cantilever motion during the scan, typically either by monitoring vertical deflection or the amplitude. The user specifies a set value to be maintained, referred to as either *deflection setpoint* or *amplitude setpoint*. The difference between the setpoint and the actual deflection is measured and referred to as the *error*. This error is scaled by the *gain*, and this signal is used to control the Z drive of the scanner. The resulting system keeps the cantilever motion constant as the tips scans along in contact with the surface.

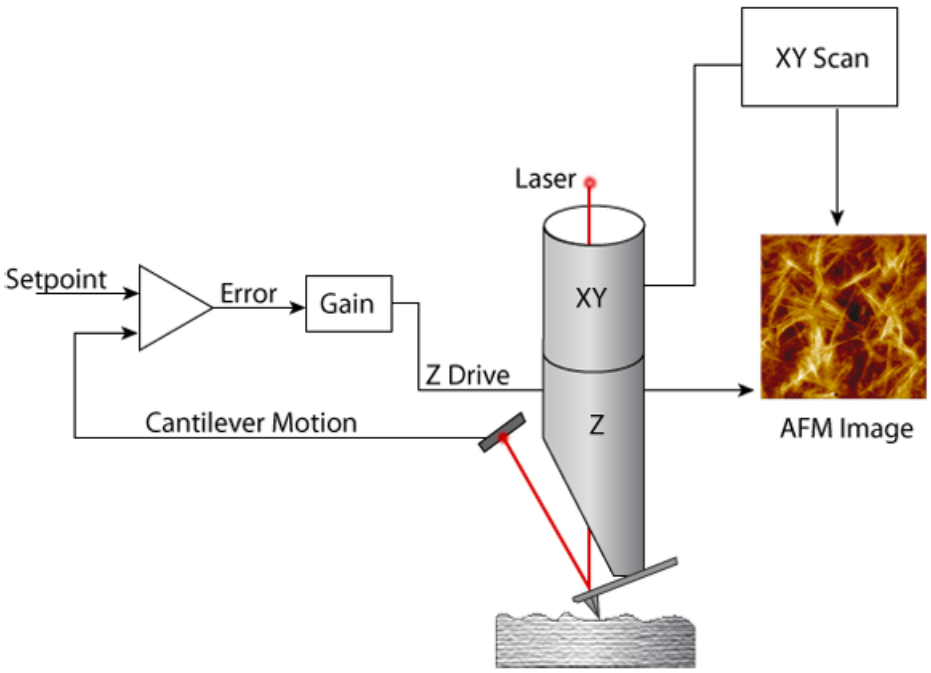

Figure 1.3.3: *Schematics depicting feedback loops in xy and Z to generate an AFM image (Adapted from [34]).*

If the gain is too low, the system will not respond fast enough to changes in the sample topography, resulting in poor quality image. If the gain is set too high, the feedback loop will become unstable and the image will appear noisy.

In order to scale the error properly, minimizing it so that the system responds accurately to changes in topography proportional and integral gains are used (PI-controller). This system allows the AFM to generate detailed topographic images of a certain surface and collect data about physical properties of the sample, such as elasticity, adhesion and roughness.

1.3.3.1 Contact Mode

In contact mode the AFM tip is brought into direct contact with the surface of the sample. Being in *direct contact* means that the force between tip and sample is in the repulsive regime. The base of the cantilever is moved up and down over higher and lower parts of the sample respectively. The force applied by the cantilever depends on the deflection, which is the parameter used by the user as a setpoint. A PI-controller processes the error in the deflection of the cantilever in order to change height position of the cantilever. The problem associated to this mode are the influence of capillary forces and the fact that lateral forces that take place as the tip scans the surface might remove material of a specific zone of the sample .

1.3.3.2 Intermittent contact or Tapping Mode

Tapping mode is another way to operate the control system of an AFM, and consists of forcing the cantilever to oscillate near its resonant frequency. In this case, the amplitude of oscillation of the cantilever is the setpoint specified by the user. As the cantilever scans the surface, it makes intermittent force-repulsive contact with the sample. The feedback loop applies a corresponding voltage to the piezo to move the cantilever vertically in order to recover the setpoint amplitude. As the cantilever is brought closer to the sample the attractive force cause a decrement in the cantilever resonant frequency, which makes it useful to deliberately set the drive frequency of the cantilever slightly lower than its natural resonant frequency. This increases the efficiency of the energy transfer so that the cantilever oscillates with greater amplitude than it did in free space [35].

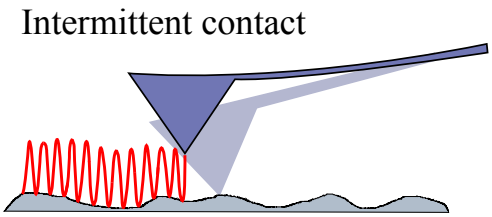

Figure 1.3.4: *Schematics of the AFM intermittent contact mode. The trayectory of the tip results from the combination of a drive frequency and the response of the feedback loop to changes in the interaction forces with the sample. The tip barely touches the sample which results in lower lateral forces (Adapted from [33]).*

One of the advantages of tapping mode is that the tip is not in contact with the surface for most of the oscillation cycle. Therefore, lateral forces generated when the tip is brought closer to the sample can be much lower than in contact mode. Moreover, when tapping is performed in air, stiffer cantilevers of resonant frequency of 200-400 Hz and spring constant of more than 10 N/m can be used in order to break free of capillary forces, improving image stability. On the other hand, when performed in liquid, capillary forces are not a problem and softer cantilevers can be used.

1.3.3.3 Non-contact mode

In non contact mode the cantilever oscillates close to the surface of the sample, but it does not make contact with it. This mode is not so widely used, since the attractive force means that there is a possibility of the tip jumping into contact with the surface. Furthermore, capillary forces makes this mode particularly difficult to control in ambient conditions and thus very stiff cantilevers are needed so that the attraction forces do not overcome the spring constant of the cantilever.

1.3.4 Force spectroscopy

Besides its capability to generate hight-resolution images, the AFM is a powerful tool for sensitive force measurements. Physical properties of the sample can be obtained changing the separation between the tip and the sample's surface at a specific location, rather than scanning the lateral position of the tip. In this

particular mode, the cantilever is only moved vertically using the piezo and then it is retracted and its deflection is measured. The small tip radius (between 5-50 nm) allows for probing a small interaction area, giving the AFM the high sensitivity to short and weak forces. This process is known as force spectroscopy.

The data from an experiment using force spectroscopy is often displayed as a bidimensional graph. The horizontal axis stands for the vertical position, and the cantilever property being measured is the vertical axis. Typically, the deflection of the cantilever gives a direct measure of the interaction force. There are two curves created, corresponding to an approach curve and a retract curve, which conform the so-called *force-distance* curve or *force curve*.

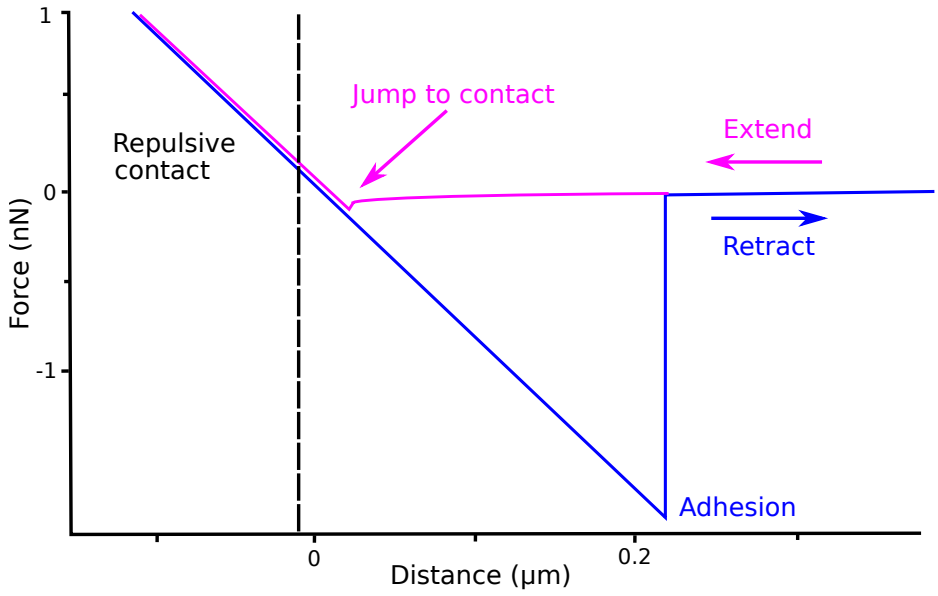

Figure 1.3.5: *Typical force-distance curve depicting approach and extend curves in air (Adapted from [33]).*

The basic force curves can be interpreted by imagining the cantilever, in air, approaching an incompressible surface such as silicon or mica (see Fig. 1.3.5) . Initially, the tip and the sample are separate enough so that initially the forces are too small to deflect the cantilever. This is the part of the extend (approach) curve that exhibits almost a null slope. At some point, the attractive forces (usually van der Waals and capillary forces) overcome the cantilever spring constant and the tip jumps into contact with the surface. As the tip-sample separation decreases

further, an increment in repulsive force is observed due to the overlapping of the electron orbitals of the sample and the tip. As the cantilever is retracted from the surface, the tip usually remains in contact with the surface due to adhesion forces and the cantilever is deflected downwards. At some point, the force from the cantilever will overcome the adhesion and the tip will break free.

From the pioneering measurements by Dufrene et al. [36, 37], force spectroscopy experiments have allowed to gain insights into the nanomechanical properties of lipid membranes at the nanometer / nanonewton scale, and thus our principal concern with force curves is the possibility to extract nanomechanical information such as the elastic modulus of the phospholipid membranes that we fabricate in the laboratory.

1.3.5 Quantitative Imaging

The traditional imaging modes explained before have well-known drawbacks, especially for samples with steep edges, as well as those that are soft, sticky or loosely attached to the substrate [38]. In contact mode, high lateral forces can damage or stretch soft biological objects. In intermittent contact, undesired forces can compress too much the sample and, furthermore in this mode, it is not possible to control the absolute vertical force, which can lead to complications on sticky samples [39].

The extend curve from the force curves as the one seen in Fig 1.3.5 can be fitted with an appropriate geometric model to obtain information about the sample deformation and its elastic modulus. On the other hand, the retract curve may be used in order to calculate the adhesion force.

Since the development of Force Volume (FV) mode in 1994, it became possible to obtain force curves related to the interaction between AFM tip and the sample [40]. In this mode, the tip approaches the sample surface until a certain maximum or peak force is reached and then it is retracted and moved to a next position. This process is rather time consuming, especially when one wants to obtain several measurements and a high-resolution image. The solution to this

problem has come recently and it is been implemented by several AFM firms with very subtle differences. Specifically, *JPK Instruments* has developed a multi-parametric mode, called Quantitative Imaging (QI) [41], which allows the user full control over the tip-sample peak force at every pixel of the image, thus providing quantitative data such as adhesion or mechanical properties of the sample, besides topographic information. This is achieved by a new algorithm which prevents lateral forces and controls vertical forces, making non-destructive imaging and fast scans straightforward.

The novel tip movement algorithm in QI mode measures a real and complete force-distance curve at every pixel of the image. This gives information about the local tip-sample interaction with high spatial resolution. The following image shows a rather simplified representation of the tip movement:

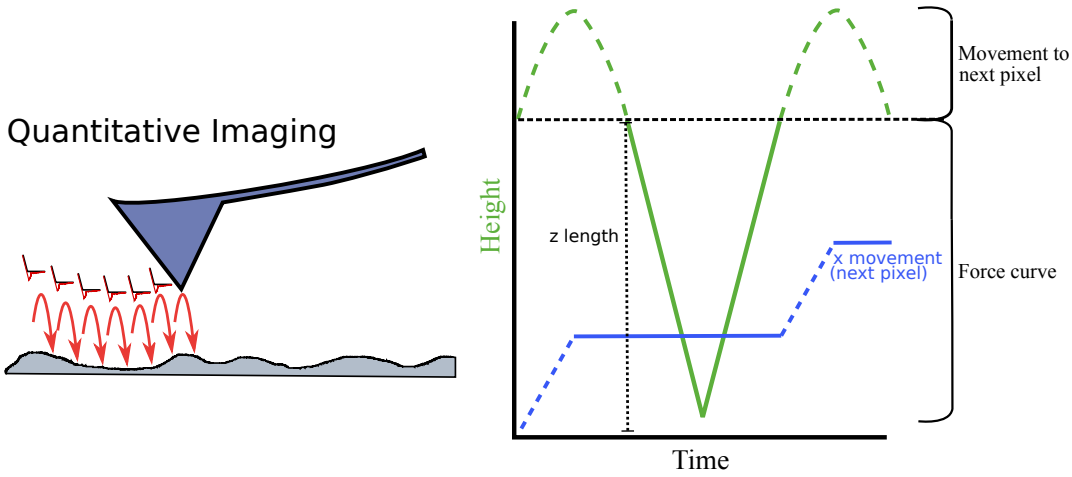

Figure 1.3.6: *Schematic view of the QI tip algorithm. The green line displays the z movement of the cantilever, whereas the blue line symbolizes the x movement. A complete force-distance curve is recorded while there is no xy movement of the tip (Adapted from [42]).*

The interaction force can be controlled and minimized to picometer force scale. In addition, one can set the tip-sample separation to deal better with soft and sticky samples (e.g. bacteria or other cells). During every force-distance measurement in each pixel of the image there is no xy movement to ensure that this curve is measured under constant velocity. This is necessary for the obtention of accurate adhesion data, which depends on the velocity during a force curve [43].

In this present work, QI mode is used to obtain the Young's Modulus of several SLBs from collected force-curves at specific temperatures. The model used to fit the extend curve is described in the following subsection.

1.3.6 Elasticity measurement

1.3.6.1 Young's Modulus

The Young's modulus or elastic modulus E is an elastic property of a material, and is defined as the *stress* of a material divided by the *strain*. This is a normalized measure of the compressibility of a material. The stress σ is defined as a force per unit area applied to a material. If the force is applied normal and outward the material surface, then it is known as tensile stress. In the case it is a force acting normal and inward the material surface it is called compression. Hence, the stress is measured in units of Newton per area and is defined as:

$$\sigma = \frac{F}{A} \tag{1.32}$$

On the other hand, the strain ε is a ratio of deformation ΔL respect to the original length of the material L_0 due to an applied stress. Hence, it is a dimensionless quantity defined as:

$$\varepsilon = \frac{\Delta L}{L_0} \tag{1.33}$$

Following the definition of the Young's modulus one obtains:

$$E = \frac{\sigma}{\varepsilon} = \frac{F}{A} \cdot \frac{L_0}{\Delta L} \tag{1.34}$$

If a piece of material is compressed uniformly, the calculation of the elastic modulus is straightforward. However, for AFM measurements the indentation geometry is usually more complicated. The specific tip shape makes it difficult to measure the force and area of indentation, thus a proper fitting is required. The Hertz fit is the standard model to analyze force-distance curves to extract

the elasticity and will be the one used to analyze our measurements.

1.3.6.2 Hertz model

The slope of the extend curve after establishing the contact point is an indication for the sample elasticity, generated by making a linear fit to this extend part at every pixel. The most common and widely used fit for AFM measurements is the Hertz fit [44], although other extended models have been generated to assess other specific assumptions.

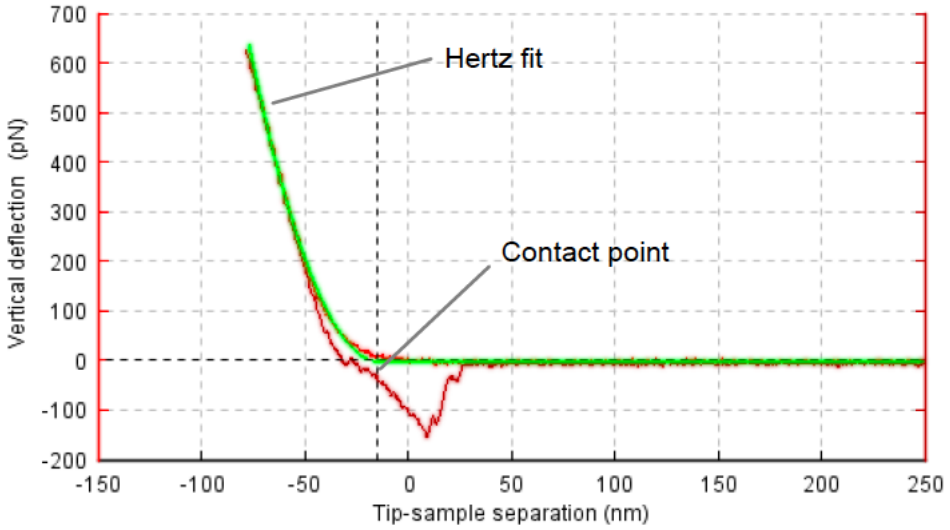

Figure 1.3.7: *Example of a force curve after baseline correction. The extend curve is fitted (in green) using the Hertz model (Adapted from [42]).*

The Hertz model approximates the sample as an homogenous and linear elastic solid occupying an infinitely extending half space. It is assumed that the indenter is non deformable and that there are no additional interactions between the indenter and the sample. If these conditions are met, the Young's modulus E of the sample can be calculated using this model. The Hertz fit relates the vertical force F with which a tip of radius R press the sample and indents the sample a distance δ, producing a deformation associated with a parameter called Poisson ratio ν, that depends on the material. The proportionality is given by the elastic modulus E of the sample:

$$F = \frac{4E}{3\left(1-\nu^2\right)} R^{\frac{1}{2}} \delta^{\frac{3}{2}} \tag{1.35}$$

The cantilever deflection Δx is first measured in volts ΔV by the quadrant photodetector, but after a proper calibration given by equation (1.37) it can be combined with equation (1.36) to account for the vertical force exerted on the sample. The relation of these quantities is coupled by the sensitivity S of the cantilever. To obtain the deformation δ of the sample one needs to establish the vertical cantilever position z, the contact point z_0 and the cantilever deflection Δx (see equation 1.38):

$$F = k\Delta x \tag{1.36}$$

$$S = \frac{\Delta V}{\Delta x} \tag{1.37}$$

$$\delta = (z_0 - z) - \Delta x \tag{1.38}$$

These equations can be replaced in (1.35) to finally obtain the Young's modulus:

$$E = \frac{3\left(1-\nu^2\right)}{4R^{\frac{1}{2}}} \cdot \frac{k \cdot \Delta V}{S\left[(z_0 - z) - \frac{\Delta V}{S}\right]^{\frac{3}{2}}} \tag{1.39}$$

The original Hertz model consider the shallow contact between two spherical bodies, but several extensions have been made for different indenter geometries . The one shown in eq. 1.35 is for a parabolic indenter which is a reasonable approximation for small indentations, it is easier to fit, and it will be used for the analysis of our experiments.

1.3.7 Calibration of the cantilever

1.3.7.1 Thermal noise calibration

The spring constant of the cantilever can be estimated from its geometry (e.g. considering thickness and width) and the properties of the material that it is made from. However, measuring the thermal noise [45] to obtain the spring constant have turned one of the most important methods of calibration since the cantilever is not damaged by the measurement. The resonance curve can be modeled with a harmonic oscillator function, as in the following formula:

$$y(f) = A\frac{f_0^2}{\left(f^2 - f_0^2\right)^2 + \left(\frac{f_0 \cdot f}{Q}\right)^2} \tag{1.40}$$

where A is the amplitude of the cantilever, f_0 is the resonance frequency and Q is the Q-factor. This is the fit used by the software to fit the resonance curve of the cantilever. The area under the curve is used to measure the amount of energy in the cantilever vibration which comes from the natural thermal environment of the cantilever. On the other hand, the equipartition theorem says that the average value of each quadratic term in the Hamiltonian is given by:

$$E_{thermal} = \frac{1}{2}k_B T, \quad k_B : \text{Boltzmann constant} \tag{1.41}$$

The hamiltonian for an harmonic oscillator is:

$$H = \frac{p^2}{2m} + \frac{1}{2}m\omega_0^2 q^2 \tag{1.42}$$

where q is the deflection of the cantilever, p its momentum, m its mass and ω_0 is the resonant angular frequency of the system. The second term can be related with the thermal energy by the equipartition theorem:

$$\left\langle \frac{1}{2}m\omega_0^2 q^2 \right\rangle = \frac{1}{2}k_B T \tag{1.43}$$

As $\omega_0^2 = \frac{k}{m}$, the spring constant of the cantilever can be finally obtained from a measurement of the mean-square cantilever deflection as:

$$k = \frac{k_B T}{\langle q^2 \rangle} \tag{1.44}$$

1.3.7.2 Contact-based calibration

This method is used to convert the photodetector signal into a quantitative value of force. This is achieved by performing a force-distance curve between a plain cantilever tip and a bare substrate in order to measure the sensitivity of the cantilever. The distance swept by the cantilever deflection induces a change in the photodetector voltage which is then calibrated. Once the deflection of the cantilever is known as a distance, the spring constant is needed to convert this value into a force using Hooke's law.

As seen from the force-distance extend curve, the repulsive contact region bends the cantilever upward, and the bending is linear when the tip is brought in contact with a hard surface. This linear behavior makes it easier for the software to determine the factor for converting volts into nanometers. The measurements may then be used to calibrate the applied forces when performing the actual experiments. When the sensitivity is measured the vertical deflection signal is displayed in unit of length. The next step is to measure the spring constant using the thermal noise method described above in order to convert the deflection signal into quantitative values of force.

1.3.7.3 Sader calibration

In 1999, John E. Sader et al. presented a fast and nondestructive method to evaluate the spring constant of rectangular cantilevers [46]. This method is time-saving because there is no need to determine the sensitivity of the cantilever in advance, which requires performing a force curve on a hard surface. The Sader method of calibration relates the spring constant k directly to the plane view dimensions of the cantilever, its fundamental mode of resonant frequency ω_f and

the quality factor of the cantilever in a fluid.

While the length of the cantilever is larger than its width, the quality factor in fluid is greater than one ($Q \gg 1$), and the thermal noise measurements are made far from the surface, then the spring constant k is calculated from the density of the surrounding fluid ρ, the cantilever's width b, length L; quality factor Q, the cantilever resonance frequency of the fundamental mode ω_f, and the gamma function Γ_i evaluated at ω_f:

$$k = 0,1906 \cdot \rho b^2 LQ \cdot \Gamma_i \left(\omega_f\right) \omega_f^2 \tag{1.45}$$

The JPK Nanowizard 3 software provides the Sader based calibration method as well as the application of correction factors to counteract the systematic errors in the measurements of the thermal noise analysis.

1.4 Raman spectroscopy

Raman Spectroscopy is a widely-used technique within the area of Condensed Matter Physics. It is used to analyze molecular vibrations of interest and it is related to the process of light scattering. When an incident monochromatic beam of light reaches a transparent material, most of the light with frequency ν_0 is scattered without any changes and only the frequency of a small fraction of light is modified. The spectra of modified frequencies $(\nu_1, \nu_2, \nu_3, \ldots, \nu_n)$ is called *Raman spectra*. In general, Raman shifts $\Delta\nu$ do not depend on the frequency of the incident beam. Hence, if a beam of any frequency is incident on a sample, one will always obtain the same Raman shifts.

The energy of photons is given by $E = m\nu$, thus, the energy of the beam would be $E_0 = h\nu_0$ which is known as Rayleigh Energy. If an incident photon strikes the sample inelastically, there is an energy transfer from the photon to a molecule of the sample. This energy transfer excites the molecule for a short period of time up to a higher vibrational and rotational energy level. When the system returns to a lower state of energy it emits a photon, the energy of which could

be higher or lower than the one from the incident photon ν_0. If the frequency of the emitted photon is less than ν_0, then it has a frequency of $\nu_0 - \nu_n$ and this downshift process is known as Stokes-Raman scattering. If the frequency of the emitted photon is bigger than ν_0, then the backscattered photon has a frequency $\nu_n + \nu_0$ and this upshift event is known as Anti-Stokes Raman scattering. After the scattering event, the molecules of the sample which interacted with the incident photons are in a different rotational or vibrational state. Each material has a set of characteristic frequencies ν_n.

Chapter 2

Experimental Procedures

In this chapter, we will explain the experimental setups used throughout this work to generate supported phospholipidic membranes and to assess the change in their elastic properties under variations of the temperature in water. The methods to characterize the samples are explained as well. The supported lipid membranes were generated by physical vapor deposition of DPPC, DMPC and DSPC, independently. The deposition thickness was monitored by very high resolution ellipsometry and the analysis of the elastic properties of the samples was made using an AFM in QI mode.

2.1 Sample Fabrication

2.1.1 Cleaning process

Squared pieces of about 1 x 1 cm are cut out from a double-polished silicon wafer and will serve as the supporting matrix of the phospholipid. The cleaning of these samples was made following the Tidswell method [47]. This procedures consists in diping the substrates in an acid solution called *piranha*. In a beaker a mixture of H_2SO_4 (sulfuric acid 95-97%) and H_2O_2 (oxygen peroxide 30%), both acquired from Merck, is prepared using a 7:3 ratio. The piranha solution is heated up to 90^oC and the substrates are immersed with the polished surface facing upwards. The substrates are held simmering in the solution for 40 minutes so as to remove

all the organic matter deposited on their surface. This process allows for the deposition of hydroxyl -OH groups on the surface of the substrates, thus making them hydrophilic. The substrates were taken out of the acid bath and deposited into a beaker with ultrapure water in the same configuration. Then, they were sonicated for eight minutes in order to remove part of the acid over the polished surface. This final process is repeated in a different beaker to dilute even more the small amounts of acid in the substrates. The substrates are finally kept under ultrapure water in a closed vase.

Before using a substrate for phospholipid deposition, it is dried under a jet stream of ultra pure nitrogen gas (99,995% of purity)(AGA/Linde, Santiago, Chile) and put onto the sample holder with the polished face upwards. Then the holder is coupled to the vacuum/evaporation chamber, which is part of the PCSA configuration for null ellipsometry. Before evaporation, the characteristic *polarizer* (P) and *analyzer* (A) values of the substrates are measured to proof their correct cleaning.

2.1.2 Physical vapor deposition of the phospholipids

2.1.2.1 Evaporation chamber setup

Depositions of a single phospholipid were made inside the evaporation chamber, using the technique of *physical vapor deposition* (PVD) . The evaporation chamber is connected to both a rotatory pump and a turbomolecular pump, which provide the level of vacuum necessary to proceed with the evaporation. Within the chamber (see Fig 2.1.1) there is a metallic Knudsen cell which contains the phospholipid to be heated and evaporated. This cell has a small hole through which the phospholipid in the gas phase exits the cell and reaches the surface of the substrate by diffusion .

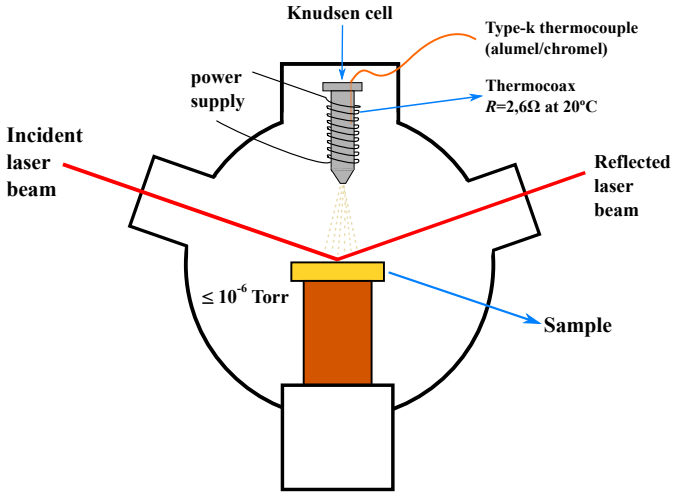

Figure 2.1.1: *Schematics of the evaporation chamber. The Knudsen cell points directly to the surface of the sample and the phospholipid is heated inside the cell. Upon heating, the phospholipid molecules evaporate and reach the substrate by diffusion (Adapted from [48]).*

The heating of the Knudsen cell is achieved by using a *Thermocoax*® resistor which surrounds the cell and through which a current is run by a power supply. The phospholipids used in this work are DPPC, DMPC and DSPC (Avanti® Polar lipids, inc.) and each evaporation follows the same steps. We fabricated nine samples of DMPC, three samples of DPPC and two samples of DSPC.

A phospholipid was deposited in its crystalline form into the Knudsen cell, which was inserted in the thermocoax resistor (see Figure 2.1.1). The system is closed in order to start the vacuum. A turbomolecular pump, assisted by a rotatory pump, is turned on and suck out the air inside the chamber until the vacuum level reaches $10^{-6} - 10^{-7}$ Torr.

2.1.2.2 VHRE-controlled evaporation procedure

Once an a optimal level of vacuum is reached, the initial polarizer and analyzer angles are measured using a *Very High Resolution Ellipsometer* (VHRE). A helium-neon laser of wavelength $\lambda = 632,8$ nm is run through the setup, which consist of the PCSA system described previously (sec. 1.2.4) and an optoelectronic feedback system (FS). The FS measures *in situ* changes of the thickness of a thin film being deposited on a reflecting substrate with an average resolution

of $0,01$ Å.

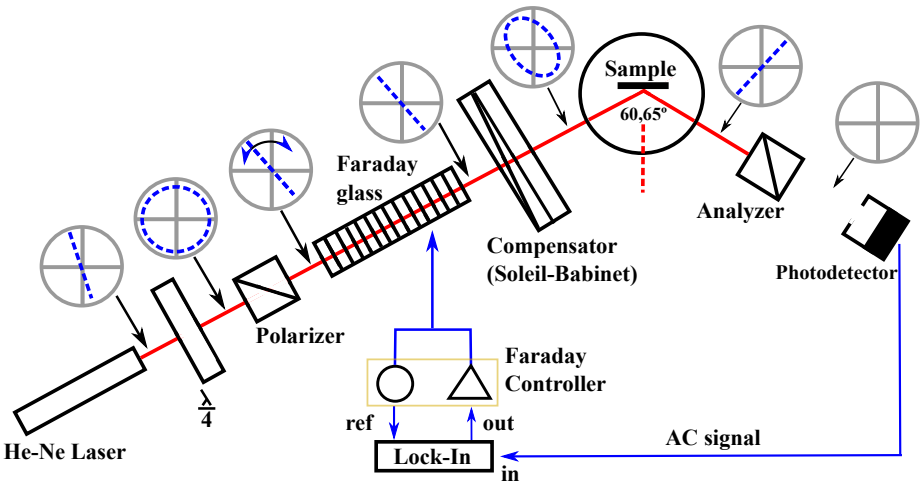

Figure 2.1.2: *VHRE setup at the Surflab UC (Adapted from [48]).*

The red beam goes through the linear polarizer and a Soleil-babinet retarder, falling with elliptical polarization on the sample at an angle of 60,65º. The reflected beam is again linearly polarized and its intensity was minimized by the analyzer until a current of a few nanoamperes was generated at the photodetector. The minimization of intensity corresponds to an initial configuration of polarizer and analyzer (P_0, A_0). After this, our power supply was turned on, and a current of 1,4 A runs through the thermocoax resistor to heat up the phospholipid in the Knudsen cell. The temperature of the cell and phospholipid was monitored by a chromel/alumel thermocouple.

Usually the temperature at which a controlled deposition is achieved is 120ºC approximately. During the deposition, the VHRE system monitors the thickness of the phospholipid deposited and only the polarizer is adjusted to maintain a minimum intensity in the photodetector. This is done until a final deposition thickness of 60Å , corresponding to a configuration $\left(P_f, A_0\right)$ with $P_f = P_0 + \Delta P$, is reached. The value of ΔP is given by the refraction index of the DPPC $n = 1,47$, and which we assume is similar for DMPC and DSPC.

2.2 Characterization

2.2.1 Raman spectroscopy

To ensure that during the evaporation process no degradation or decomposition of the phospholipids occur, we analyzed PVD-thick-films of DMPC, and DSPC of about 500 Å or more using Raman spectroscopy and then compared them with the spectroscopic results for the bulk material analyzed out of the box. Hence, structural and vibrational properties of certain functional groups of these phospholipids were characterized with a Micro Raman System *LabRam 010* from Instruments S.A. using a 5,5mW, 632,8 nm He-Ne laser in combination with a visible light spectrometer and an Olympus optical microscope. Data acquisition time was 20 s. A Raman characterization for DPPC has already been performed in [18] giving positive results.

2.2.2 Atomic Force Microscope

2.2.2.1 General setup

A commercial AFM NanoWizard® 3 from JPK Instruments located at the Material Science laboratory of he Pontifical Catholic University of Chile (*Surflab UC*) was used to obtain information about the topography and the elastic modulus of the samples.

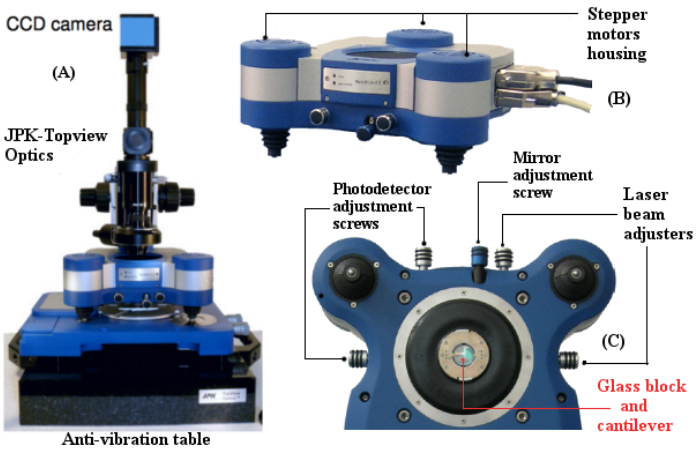

Figure 2.2.1: *(A) Image of the AFM NanoWizard 3 from JPK Instruments. (B) Side view of the AFM head. (C) Bottom view of the AFM head (Adapted from [33]).*

The AFM body is mounted on an isolation table in order to prevent external vibrations that could alter the experiments. The body consists of a TopView-Optics system which allows to focus the surface of a sample using a CCD camera. The AFM head features three piezoelectric Z-stepper motors, which level the height of the head respect to the sample, and micrometer adjusters for the mirror and quadrant photodetector. Silicon nitride cantilever chips (*Nanosensors*®) were clamped to a glass block which is coupled to the bottom of the head (this is the scanner configuration). The glass block can be mounted or removed whenever one needs to change the cantilever or clean the glass block.

A semi-open cell system consisting of a Peltier device is the base on which the samples were attached using a bicomponent epoxy resin. The Peltier device is connected to a heating-cooling module (HCM) from which a temperature of resolution 0,1^{o}C can be set within a range between 0^{o}C up to 80^{o}C in aqueous solutions. To prevent an overheating of the cell, a water pump stage makes water run through small pipes around the Peltier device. As the temperature shown by the HCM is not exactly the same as the one in the surface of the sample, a thermocouple was placed on the surface of the sample (see Fig. 2.2.2).

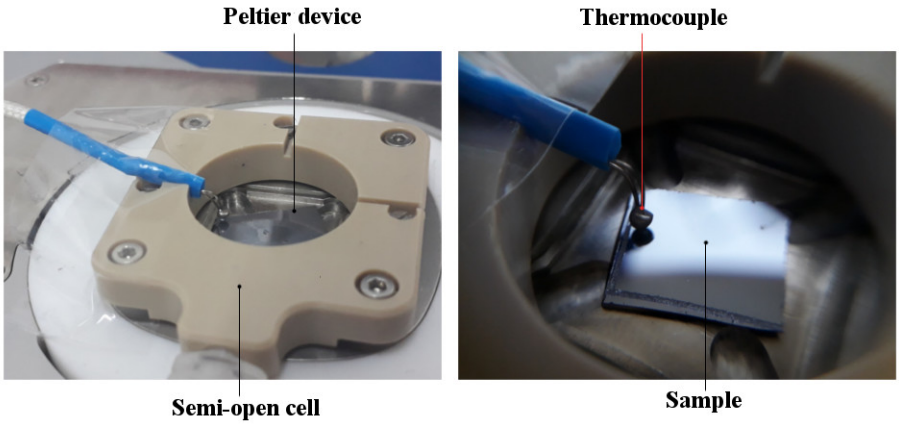

Figure 2.2.2: *On the left: semi-open cell in which the water environments is held. The base of the enclosement is a Peltier device that changes the temperature of water. On the right: the interior of the cell is shown. A sample is glued at the Peltier and a thermocouple is put on the surface to measure accurately the temperature of the sample.*

The cell allows the sample, together with the cantilever and part of the glass block, to be submerged in the water during the experiments.

2.2.2.2 Adjustment of the detection system

For the calibration of the cantilever one has to make sure that the laser detection system is set up. For this, we adjusted mirror so that the laser beam could point towards the quadrant detector. Then we placed the laser spot onto the end of the cantilever and centered the beam in the detector to give maximum sensitivity for imaging and force control. All this information is checked *in situ* by the software and displayed on a computer screen.

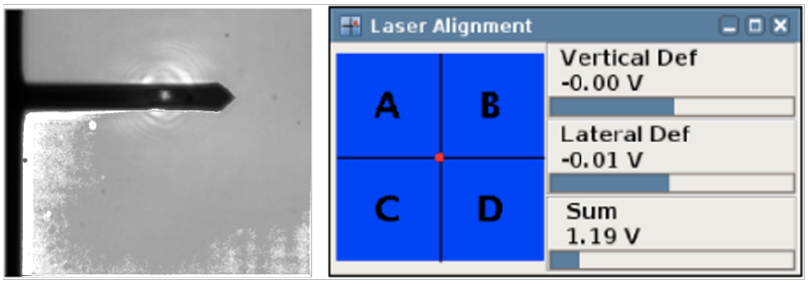

Figure 2.2.3: *On the left: Top view of the cantilever and the laser spot on it. On the right: The information displayed by the JPK software about the centering of the laser spot on the quadrant photodetector (Adapted from [33]).*

2.2.2.3 Calibration of the cantilever

We used to obtain the sensitivity and spring constant of the cantilever we used respectively the contact-based mode and the thermal noise method. However, we updated the JPK software lately and some of these values were obtained by means of the Sader method which in practice is faster and straightforward. For the former case we simply performed a force curve on a bare silicon substrate in air and fit a line along the repulsive region of the extend curve to obtain the sensitivity of the cantilever (conversion from volts into nanometers). Finally the software fits another curve to the resonance peak of the cantilever to obtain the spring constant. We obtain a nominal constant of $k = 0,025$ N/m and a sensitivity of $S = 24,61$ nm/V. Now the system is ready to perform a scan.

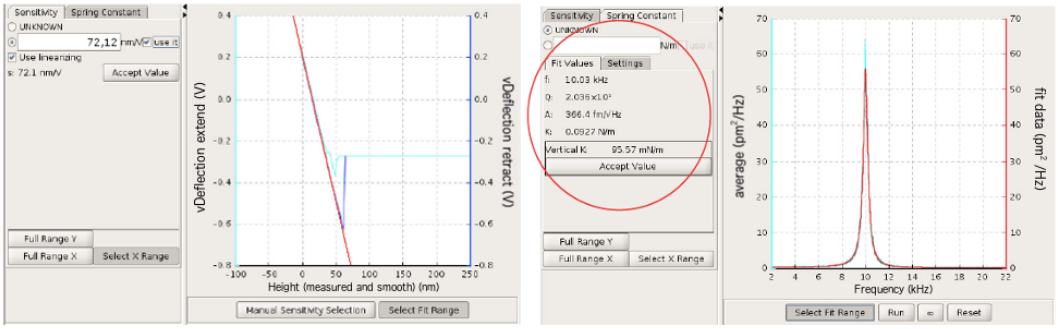

Figure 2.2.4: *The left image shows the force curve and a linear fit (red) to the repulsive region of the extend curve. The right image shows the resonance peak of the cantilever and the fit (red) associated to it (Adapted from [33]).*

In the case of the Sader method, we input the values of the width ($48 \pm 7,5$ μm) and length (225 ± 10 μm) of the cantilever and the system automatically measures the sensitivity and the spring constant.

2.2.2.4 Data obtention using QI

Before every data acquisition using QI, we performed a 100 x 100 μm^2 contact mode image to the studied samples in order to identify the areas where the phospholipid were deposited. We added MiliQ water (Merck) to the cell and

performed another topographic scan in contact mode to check if there was a shift in the position of the phospholipids during the filling. The JPK software was used to take cross sections of the topography to evaluate the thickness of the phospholipid layers deposited. We looked for depositions between 4 nm and 6 nm in height which corresponds to the reported height of one lipid bilayer. If the depositions do not meet this requirement, we just take an homogeneous extension no matter its height.

To establish the minimum force that should be used in order to avoid tip indentation in the membranes we performed several force curves, at 1nN, 5nN, and 10nN for each of the phospholipids in order to see any breakthrough event in the repulsive part of the extend curve. We obtained an interesting result on DMPC (see section 3.2) which gave a breakthrough force of 1.219 nN which established a maximum force that we lowered down to 1 nN for data obtention.

After selecting a scanning zone over the samples, images of 256 x 256 pixels and force-curves in QI mode at 1nN peak-force were taken at the same time, covering an area of 100 x 100 nm^2 or 200 x 200 nm^2. The position of the cantilever was set to $z = 190$ nm and the image areas chosen were much lower than the area of lipid deposition in order to satisfy the condition for homogeneity of the Hertz model. All the force curves were performed being the sample at or near a thermal steady state, provided by the constancy in the thermocouple reading of the sample's temperature. We started from 10^oC and each subsequent zone-scanning was performed in increments of 2^oC, until the temperature of the sample reached 50^oC or 60^oC.

2.2.2.5 Data processing

From every QI mode data obtained, we used the JPK software to batch-process all the force curves obtained from each pixel in the scanned area. The batch process consisted in applying a Hertz fit to every extend force curve to obtain a histogram which shows the number of events for the Young's modulus of a sample at a fixed temperature. To each of these histograms (i.e. for each temperature),

a two-gaussian fit is adjusted using ORIGIN 8.0 and then the maximum value of the gaussian curve which fits best to the histogram is selected. Finally, the elastic modulus data obtained from the fitting process is plotted as a function of the sample's temperature.

Chapter 3

Results and discussion

3.1 Raman spectroscopy

Before collecting any kind of data with AFM, it was necessary to assess whether the molecular structure of the phospholipids remained the same after the deposition. The phospholipids are subjected to a temperature higher than 100^{o}C during PVD, which is two or three times higher than the temperature that most biological membranes are exposed to in their natural ambient.

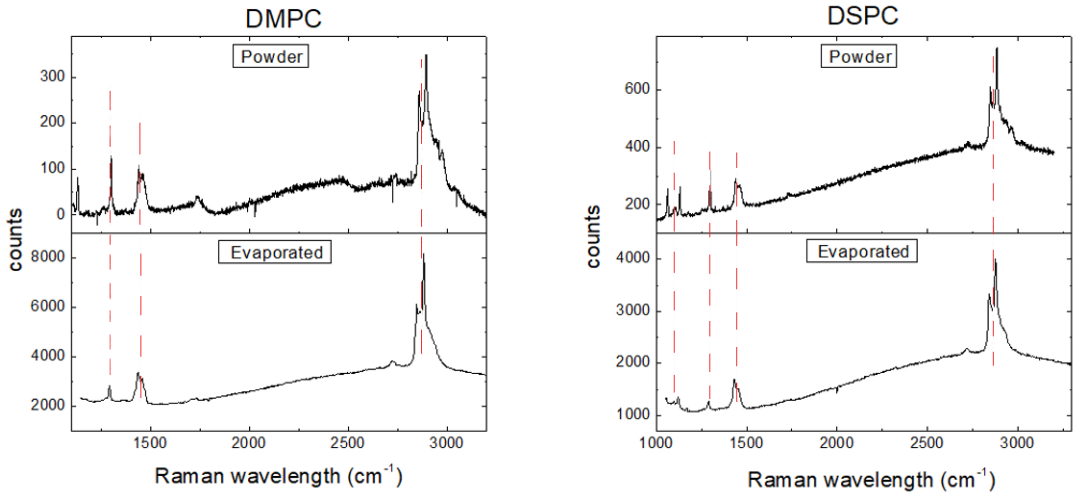

Figure 3.1.1: *Raman spectra for DMPC (left) and DSPC (right). Powder spectra correspond to the phospholipids taken from their original package.*

The Raman spectra shown in the graphs feature the spectra for phospholipids

analyzed just as they come in their original package (named *powder*); and for the ones evaporated by PVD onto a silicon substrate. From the work of Retamal et al. [18], we know that DPPC does not change its molecular structure. For the case of DMPC and DSPC, the graphs show that the characteristic peaks for both phospholipids are all coincident with the ones evaporated onto the substrate. Thus, we can be certain that the molecular structure of both phospholipids remains unaltered after PVD.

3.2 Breakthrough force

The following image shows the result of the single force curve made to a DMPC sample. It is seen that when the cantilever is away from the sample, no interaction between the tip of the AFM probe and the sample is observed. As the tip approaches to the sample it begins to interact with the surface. No capillary force is observed before the contact point because the bilayer is under water. The initial repulsive regime comes from a varying nature of forces, which are highly dependent on the bilayer chemistry or the one of the AFM probe.

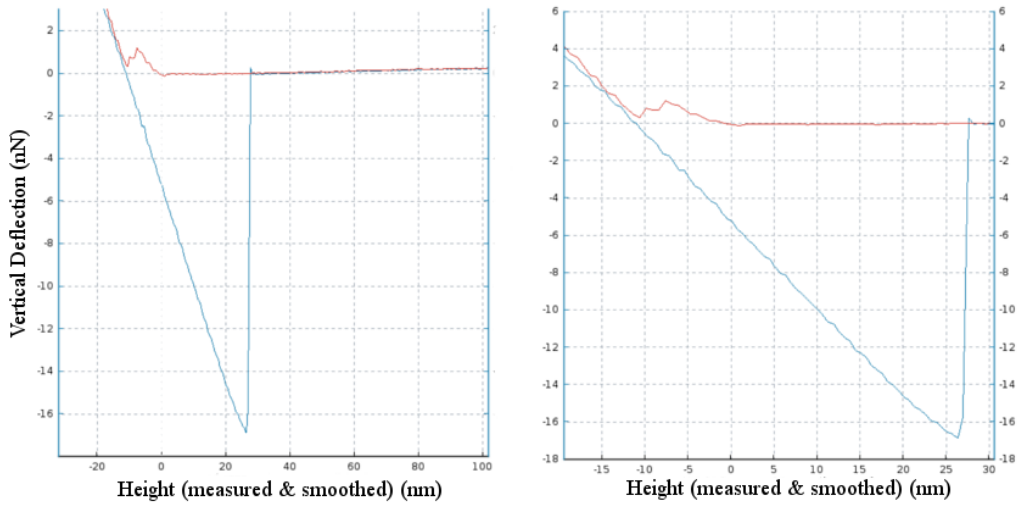

Figure 3.2.1: *On the left: The extend force curve (red) exhibits a kink at* 1,219 nN *in the repulsive regime which accounts for the membrane rupture. On the right: A close-up of the graph shows the extent of indentation.*

A kink can be seen in the extend red curve and we believe that it is caused

when the applied force reaches a threshold value and the tip indents the DMPC membrane. The breakthrough force measured by the JPK software is 1.219 nN which is in accordance with the measurements made by Dufrene et. al [37] showing that the force required to trigger an elastic-plastic transition on a lipid bilayer occurs in the nanonewton (nN) regime. We are not sure of penetrating the whole bilayer since the jump measures $2,91$ nm which is less than the 4 nm reported thickness of a bilayer as revealed by other AFM images [21]. However, this result is in agreement with the indentation experiments of Volker et al. using DOTAP [49], which is similar in length to DSPC.

Anyway, this breakthrough event marks the penetration of the cantilever tip through the DMPC membrane, and features the onset of the plastic deformation regime. The indentation force identifies clearly the maximum force that the membrane is able to withstand before being penetrated by the tip.

Identifying this threshold force allowed us to place un upper limit to the maximum set-point force to the bilayer in order to stay in the elastic regime, which is crucial to obtain the data for the Young's modulus. We also see that in the presence of a plastic deformation the contact line of the retraction curve does not overlap with the approach contact line. This shows that, upon retracting of the tip, the sample does not retain completely its shape.

3.3 AFM topography

The contact mode images show that the phospholipids are able to cover certain areas of the substrate in an non-uniform manner. The molecules also tend to aggregate in *islands* of several bilayers, as shown in the next images.

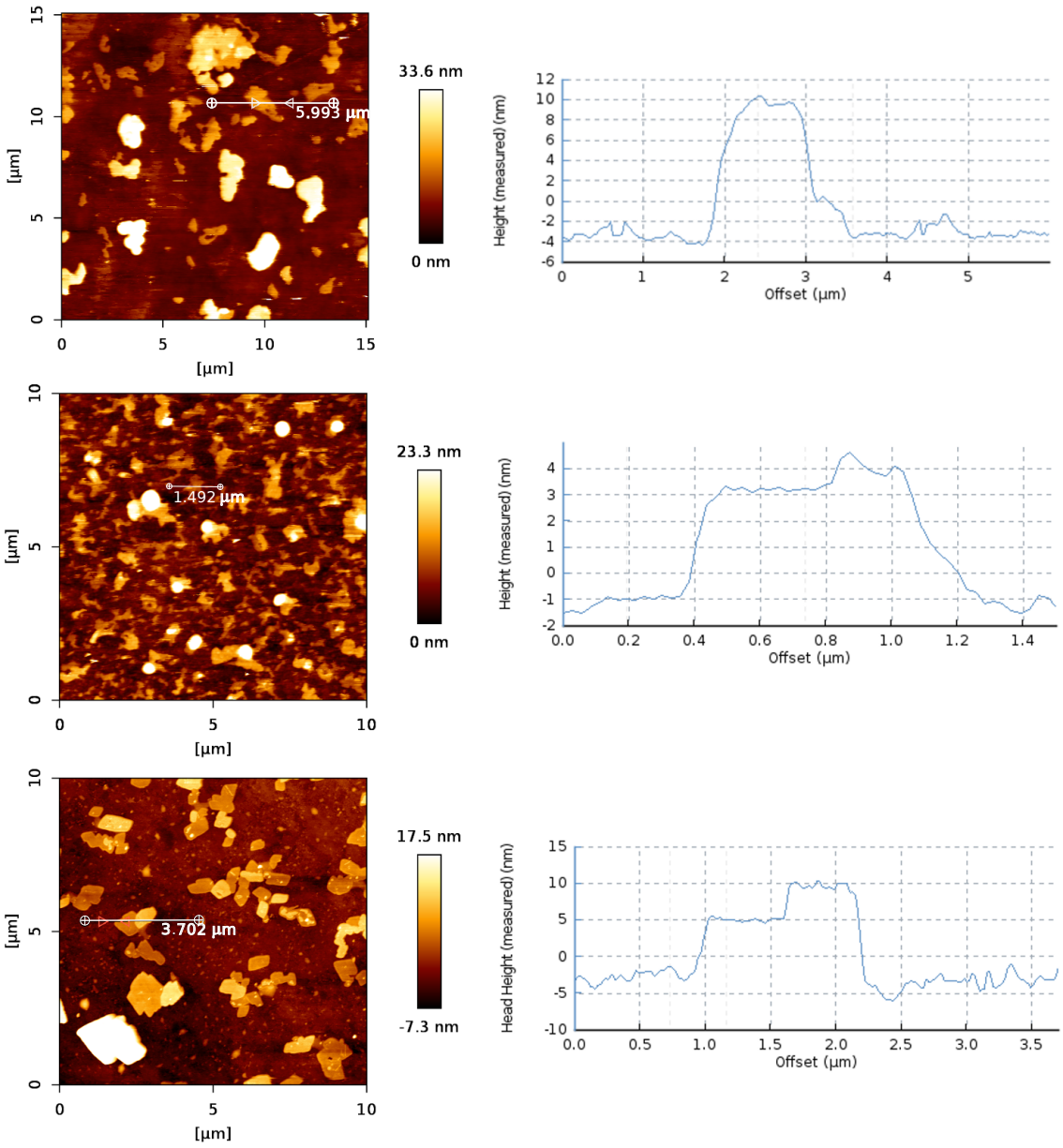

Figure 3.3.1: *Contact mode images and one respective cross-sections (T-B): DMPC, DPPC, DSPC.*

We show cross sections of some accumulation of phospholipids and we mostly see throughout our experiments that it seems difficult to find single bilayer extensions for the three phospholipids. Hence, we tried to assess whether a multilayer extension was suitable for a QI-mode scan by trying to find the islands that have the least number of bilayers. Then, we scanned a smaller center area of 100x100 nm^2 portion of one island in QI-mode.

3.4 Young's modulus histogram

For each temperature measurement, we batch-processed all the QI-mode force-curves taken at each pixel of the area scanned. This yielded one histogram for the Young's Modulus for each temperature of a sample. Most of the graphs obtained depict a distribution with a peak of the order of the MPa, and some of them present interesting features at the main gel-to-fluid transition temperature.

The next graphs depict two histograms generated for a DMPC sample with a two-gaussian adjust, as if there were two phase states contributing to the elastic properties of the sample. The two gaussians are added and then we took the maximum value of the cumulative peak as the value of the Young's modulus of the membrane. We see that at 24ºC the DMPC island corresponding to an average height of 7.78 nm, has an elastic modulus of $E = 1,490$ MPa. The cumulative fit shown in blue in Figure 3.4.1 comes from the sum of two gaussians whose peaks are at $P_1 = 1,485 \pm 0,002$ MPa (red curve) and $P_2 = 1,697 \pm 0,060$ MPa (green curve). The red gaussian is the most prominent of the two, meaning that most of the DPPC molecules are in a state corresponding to a Young's modulus given by P_1 which is very similar to the one depicted by the cumulative peak.

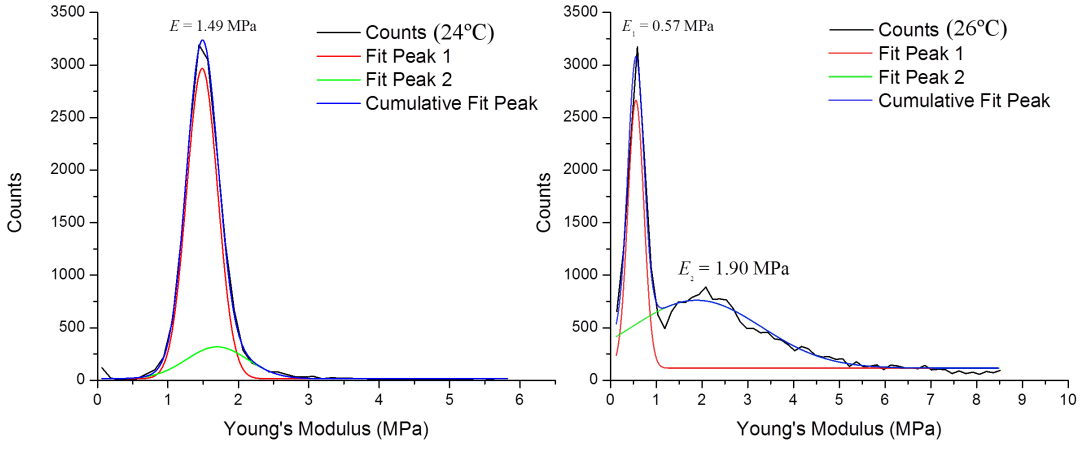

Figure 3.4.1: *Histogram for the elastic modulus of DMPC. We see that at 24ºC the elastic modulus of the membrane 1,49 MPa and at 26ºC it decreases to 0,57 MPa*

After increasing the temperature up to 26ºC, we see in the graph on the right

two main contributions for the elastic modulus. One corresponds to a sharp peak at $E_1 = 0,57$ MPa, associated with a contribution (in red) with peak at $P_1 = 0,570 \pm 0,004$ MPa, and the other corresponds to a spread distribution with a peak at $E_2 = 1,90$ MPa associated at a contribution (in green) with peak at $P_2 = 1,900 \pm 0,095$ MPa. The appearance of a second peak with a lower Young's modulus suggests that we have a phase transition. The flattened cumulative peak E_2 at 26ºC is similar in value to the single-peak at 24ºC but the counts are less. Hence, some phospholipid molecules are still in the gel phase whereas the majority have transitioned to the fluid phase. One would expect that at a higher temperature the spread peak disappeared. In fact, the next graph shows that the spread peak is absent at a sufficiently hight temperature, meaning that all the DMPC molecules are in the liquid phase.

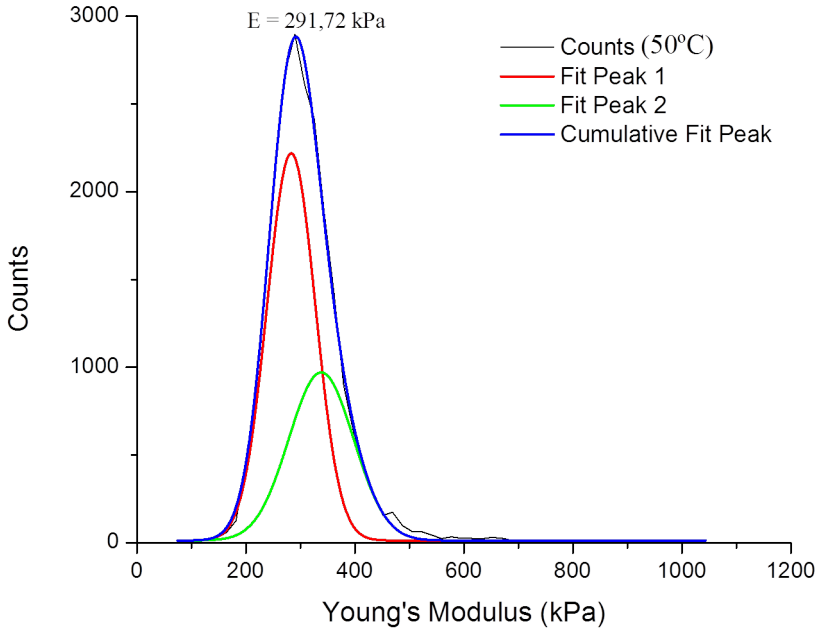

Figure 3.4.2: *Well above the main transition temperature of DMPC, all the molecules are in the liquid phase and exhibit a lower elastic modulus of 291,72* kPa.

In this last case, for a DMPC sample at 50ºC, the cumulative fit features a peak corresponding to an elastic modulus of $E = 291,72$ kPa. The gaussian

contributions are $P_1 = 283,19 \pm 5,21$ kPa and $P_2 = 338,13 \pm 68,99$ kPa. The change in the elastic scale from MPa to hundreds of kPa depicts a softening of the area scanned.

In the case of DPPC, we were able to distinguish a phase transition by observing the appearance of a second peak in the histograms upon increasing temperature above the reported main transition of 41ºC. The next set of histograms was generated for a DPPC island of 9,52 nm in height within a scan area of 200 x 200 nm^2.

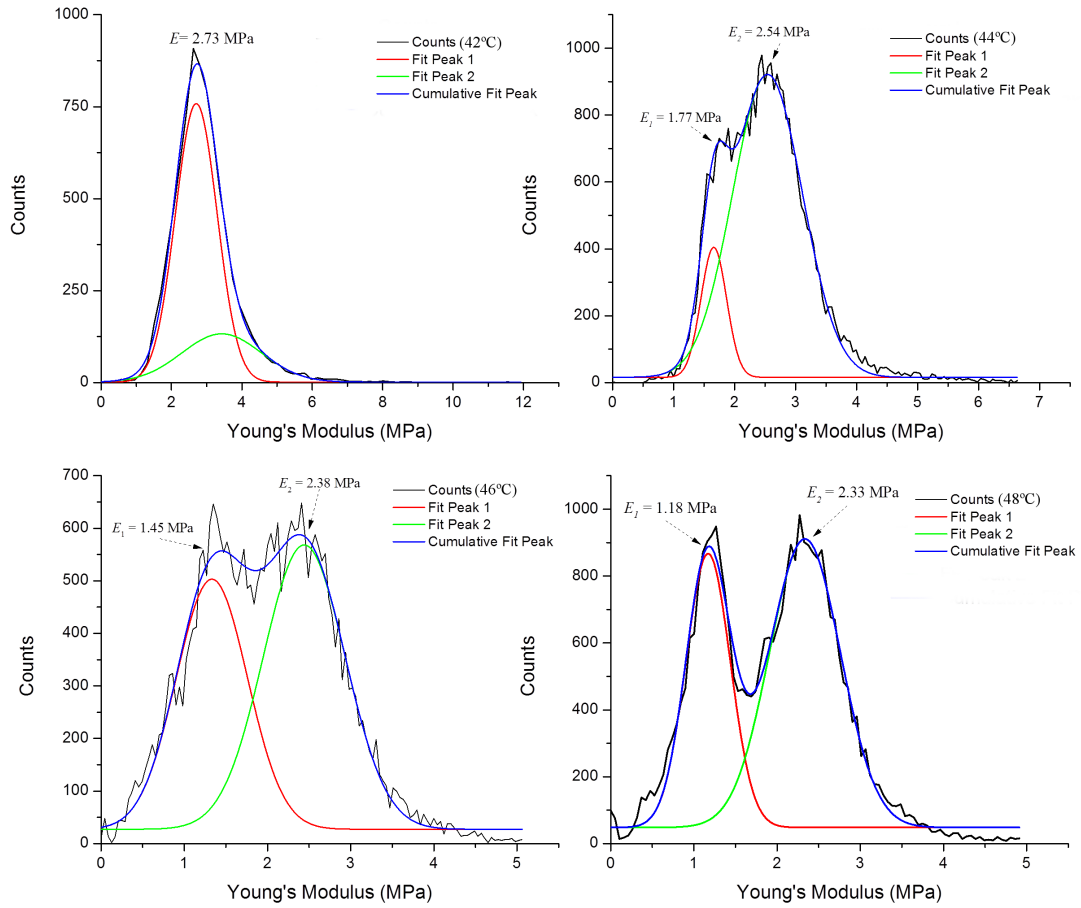

Figure 3.4.3: *Histogram depicting the phase transition of DPPC at 42ºC. The graphs show the appearance of two concurrent states. Our interpretation of these curves is that they represent the coexistence of the gel and fluid phases.*

Notice that at 42ºC all the DPPC molecules are in a gel state with elastic modulus of $E = 2,73$ MPa as seen in the blue cumulative fit (blue). This fit is given by two contributions whose average is at $P_1 = 2,705 \pm 0,011$ MPa

and $P_2 = 3,427 \pm 0,186$ MPa, showing that almost all the DPPC molecules have not transitioned to the liquid phase yet. Increasing the temperature up to 44ºC we start to see the appearance of a two-peak histogram, in which the cumulative fit exhibit a peak of $E_1 = 1,77$ MPa and a higher peak of $E_2 = 2,54$ MPa. The cumulative fit has been generated from two gaussian of average values $P_1 = 1,659 \pm 0,009$ MPa and $P_2 = 2,541 \pm 0,012$ MPa. The shape of the cumulative curve tells us that some DPPC molecules have transitioned to the fluid state with lower elastic modulus.

Further up to 46ºC and 48ºC a coexistence of the gel and liquid phase in the area scanned is observed. At 46ºC we see that the cumulative fit features two maxima $E_1 = 1,45$ MPa and $E_2 = 2,38$ MPa, and the two gaussian contributions feature peaks at $P_1 = 1,332 \pm 0,033$ MPa and $P_2 = 2,441 \pm 0,033$ MPa. At 48ºC we clearly distinguish that half of the area scanned exhibit a lower elastic modulus corresponding to $E_1 = 1,18$ MPa, well fitted by the red gaussian $P_1 = 1,171 \pm 0,008$ MPa. The DPPC molecules which contributes to this value of the elastic modulus have transitioned to the fluid phase, whereas the rest of the molecules still in the gel phase give an elastic modulus of $E_2 = 2,33$ MPa related to the peak $P_2 = 2,335 \pm 0,009$ MPa. The next table summarizes the values for the elastic modulus for these DPPC histograms.

T(ºC)	Cumulative Fit Maximum (MPa)	Peak 1 (MPa)	Peak 2 (MPa)
41	$E = 2,73$	$2,705 \pm 0,011$	$3,427 \pm 0,186$
44	$E_1 = 1,77$	$1,659 \pm 0,009$	–
	$E_2 = 2,54$	–	$2,541 \pm 0,012$
46	$E_1 = 1,45$	$1,332 \pm 0,033$	–
	$E_2 = 2,38$	–	$2,441 \pm 0,033$
48	$E_1 = 1,18$	$1,171 \pm 0,008$	–
	$E_2 = 2,33$	–	$2,335 \pm 0,009$

Table 3.1: *Values of elastic modulus of DPPC near the main phase transition temperature. The cumulative fit is the sum of two gaussian curves with average values denoted by Peak 1 and Peak 2.*

We expect that all the molecules of DPPC transition to the fluid phase at a sufficiently high temperature. In fact, in the next graph we show a single peak at

63ºC with a cumulative peak at $E = 0,82$ MPa. The peak is well adjusted by the gaussian fit with average value $P_1 = 0,819 \pm 0,003$ MPa. The other gaussian (in green) has an average value of $P_2 = 1,427 \pm 0,197$ MPa. However, the number of events of the red gaussian fit outnumbers the events shown by the green fit. Thus, practically all the DPPC molecules are in the liquid phase.

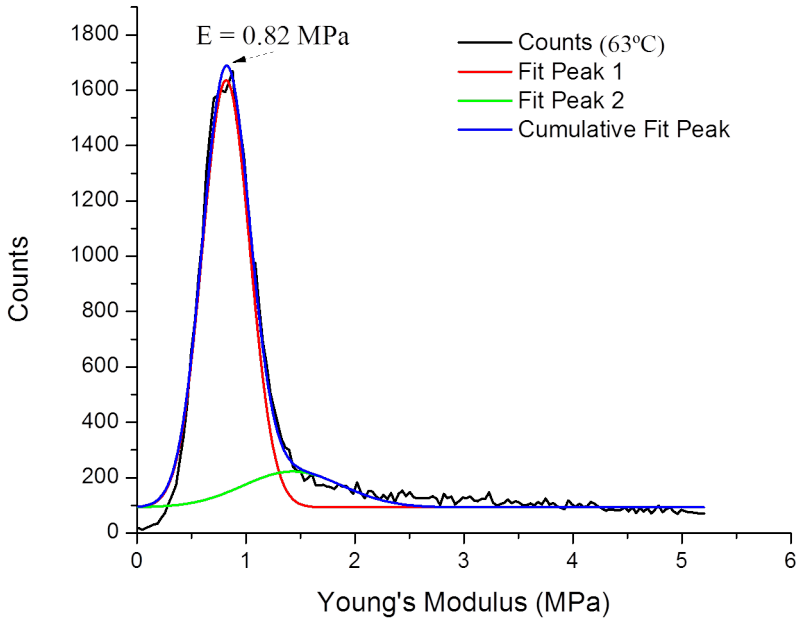

Figure 3.4.4: *Histogram for the elastic modulus of DPPC at 63ºC. The value of the elastic modulus at this temperature is around $E = 0,82$ MPa.*

3.5 Elastic modulus vs temperature

Not all the histograms depict the coexistence of the gel and fluid phases at the main transition temperature. In fact, most of them show just one peak shifting with increasing temperature. We believe that two-peak appearances might be the result of stochastic processes occurring under specific configurations of thickness, molecular cohesion, or edge effects due to sudden changes in the topography of the membrane and the expansion of the substrate at higher temperatures.

The following graphs shown in Figure 3.5.1 show the variation of the elastic

modulus upon increasing temperature for DMPC, DPPC and DSPC. The plots show that the Young's modulus for the three phospholipid studied share a similar scale in the order of MPa, provided by the use of the Hertz model. Particularly, one can observe that the DSPC membrane is stiffer in the gel phase as seen in the higher values of elastic modulus within this regime.

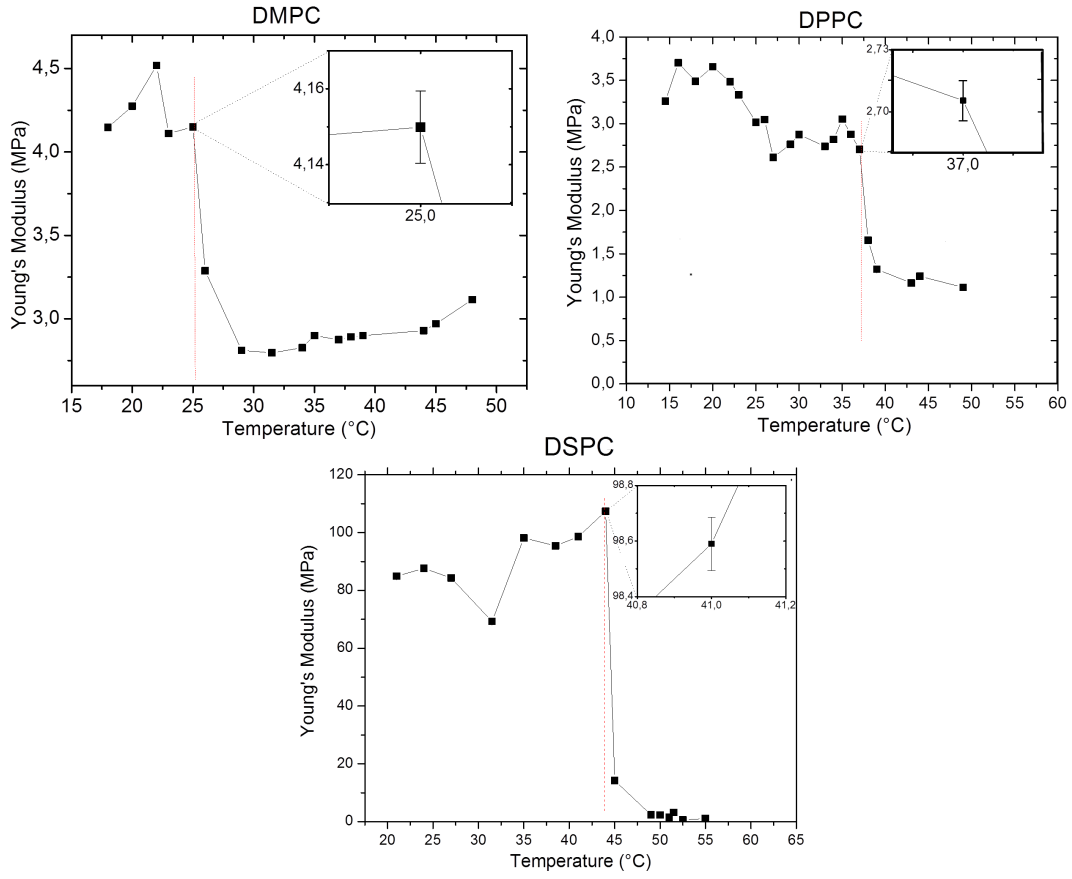

Figure 3.5.1: *Elastic modulus behavior upon changes in temperature. The three phospholipids exhibit a drop in the Young's Modulus near the gel-to-fluid transition temperature. This transitions take place at 25ºC, 37ºC,44ºC for DMPC, DPPC, and DSPC, respectively. The insets are aim to show the scale of the errors associated to the experiments.*

The standard deviations, generated from the best gaussian fit to the histogram, are not seen at first sight in the plots because their values deviate less than 5% from the mean. The inset in each of the plots depicts the scale of the deviations.

An arresting drop in the elastic modulus for the three phospholipids near

their main phase transition temperature marks the transition to the fluid state. In the case of DMPC, the temperature at which the transition is observed is at $T = 25^{\text{o}}\text{C}$, in good agreement with its reported main transition [23]. The elastic modulus for this membrane changes from $E_{_{DMPC}}(25^{\text{o}}\text{C}) = 4,150 \pm 0,010$ MPa to a minimum value of $E_{_{DMPC}}(33^{\text{o}}\text{C}) = 2,875 \pm 0,008$ MPa. We do not have an explanation for the increasing change in the Young's modulus at higher temperatures for this phospholipid. For the case of DPPC, the drop in the elastic modulus appears at $T = 37^{\text{o}}\text{C}$ and goes from $E_{_{DPPC}}(37^{\text{o}}\text{C}) = 2,710 \pm 0,010$ MPa to a minimum value of $E_{_{DPPC}}(48^{\text{o}}\text{C}) = 1,112 \pm 0,013$ MPa. Finally, for DSPC, the transition is shown at a temperature of $T = 44^{\text{o}}\text{C}$ and the drop in the elastic modulus goes from $E_{_{DSPC}}(44^{\text{o}}\text{C}) = 107,40 \pm 0,10$ MPa to a minimum value of $E_{_{DSPC}}(52^{\text{o}}\text{C}) = 0,610 \pm 0,030$ MPa.

One can notice that the scale for the Young's modulus of the DSPC is two times higher in the gel phase than the ones observed for the DMPC and DPPC. We have not found in literature a typical value for the elastic modulus of these phospholipids, since many of the AFM studies of elastic properties are performed on vesicles rather than in planar lipid membranes. Other researchers use different substrates, or different pH and ionic concentrations in the solution, which changes the mechanical properties of the bilayers and it also forces the use of other models of indentation. The only paper we found which resembles our experimental conditions gives a value of the elastic modulus of tenths of MPa for these three phospholipids in both the gel and fluid phases [50]. However, they do not use the Hertz model and use single force-distance curves to determine the Young's modulus.

Nevertheless, we expect a drop in the Young's modulus after the phase transitions of the lipids, since the translational behavior of the phospholipid molecules in the liquid phase makes the membrane more susceptible to deformations. On the other hand, phospholipids in the gel phase exhibit a cohesive behavior in which the molecules are in close contact with one another, making the membrane more stable and harder to tear apart. The change of the elastic modulus just

near the reported transition temperatures makes us think that phase changes do occur in these membranes, which ultimately establishes that bilayers are indeed assembled. This trend matches the one evidenced in [51]and in [18].

Finally, we notice that the values of the main transition temperatures for both DPPC and DSPC undershoot the ones usually reported by a few degrees Celsius. This difference may result from temperature instabilities within the cell due to evaporating water at higher temperatures. As the heating controller transfer energy to the sample, it generates a gradient of temperature in the cell. Because the cell is an open system, molecules of water near the substrate can escape the system taking out energy from it and thus a steady state of inward-outward flow of energy is established. This happens especially when working at temperatures higher than 40ºC. Above this temperature we usually had to refill the cell with ultrapure water at ambient temperature in order to keep the thermocouple under water and wait for the setting of a steady state to perform new measurements at the desired temperature.

Chapter 4

Conclusions and future work

Thin films of phospholipids DMPC, DPPC and DSPC were assembled on a polished silicon substrate using Physical Vapor Deposition (PVD) and thickness-controll by *Very High Resolution Ellipsometry* (VHRE). The evaporation process yields samples of 60Å average thickness. Raman spectroscopy for DMPC and DSPC shows that the molecular structure of both phospholipids is not altered after the evaporation over the substrate. The Raman spectra for DPPC was investigated in a previous work showing similar results. From these results we expect that a wide range of phospholipids is not afected by PVD in high vacuum.

We studied the elastic properties of these phospholipids under ultrapure water as a function of the temperature by means of Atomic Force Microscopy (AFM). The operating mode of the AFM used in this work is *Quantitative Imaging* (QI), developed recently in 2012 by *JPK Instruments*. The idea behind this mode is to select an scanning area over the sample, and perform a force-distance measurement in each pixel of the image. The scanning areas that we examined on our samples are of around 100 x 100 nm^2, covering a phospholipid island with constant height of two bilayers, with a resolution of 256 x 256 pixels.

As the number of data collected using the QI mode consists of more than 60000 force-curves for each temperature and each sample, we batch-processed this data with the Hertz model for tip indentation using the *JPK Processing Software*. We consider our cantilevers to be parabolic indenters with tip radius

of 8 nm (measured using FE-SEM), nominal spring constant of 0,025 N/m, and sensitivity of 24,61 nm/V.

From a force-curve measurement we identified a break-through event, where the tip of the cantilever penetrates a DMPC membrane with a force of 1,219 nN (given by the software). Breakthrough events were not observed for the other lipids used, even for forces up to 10 nN. Thus, we decided to establish a minimum peak-force load of 1 nN to each sample in order to collect data in the elastic regime. We identified a hysteresis between the extend and the retract curves from the break-through kink, meaning that once the plastic onset is set, the bilayer does not retain its original form.

We subjected our samples to a range of temperatures from 15ºC - 20ºC up to 60ºC - 63ºC, in increments of 2ºC. The force-distance curves obtained at a fixed temperature with 1nN peak force in QI mode were fitted using the Hertz model, which allowed for the obtention of the Young's modulus of the lipid studied. For a fixed temperature we obtained histograms depicting the number of ocurrences for a certain value of the elastic modulus of the samples. We found certain histograms for DMPC and DPPC in which we believe a certain phase transition occurs as the appearance of a two-peak histogram. The peaks depict a scale of MPa in the elastic modulus when these samples are in the gel state, but they drop to hundreds of kPa in the liquid phase. For DMPC the elastic modulus is $1,485 \pm 0,002$ MPa in the gel phase at 24ºC but it decreases to $0,570 \pm 0,004$ MPa at 26ºC. For DPPC in the gel phase, the elastic modulus is $2,705 \pm 0,011$ MPa at 42ºC and in the liquid phase is $0,819 \pm 0,003$ MPa at 63ºC. We interpret this as a softening of the studied membranes. For the DSPC we did not observe double-peak histograms.

The vast majority of the histograms obtained depicted a single peak which shifts upon increasing temperature. As a general trend for the three phospholipids, one can see that there is a softening of the membranes studied above the main gel-to-fluid transition. For DMPC, the elastic modulus in the gel phase is $4,15 \pm 0,01$ MPa at 25ºC and it reaches a minimum value of $2,875 \pm 0,008$

MPa in the fluid phase at 33ºC. For DPPC, the elastic modulus in gel phase is $2,71 \pm 0,01$ MPa at 37ºC an it drops to $1,112 \pm 0,013$ MPa in the fluid phase at 48ºC. Finally for DSPC we obtained an elastic modulus of $107,4 \pm 0,1$ MPa in the gel phase, and it drops sharply in the fluid phase down to $0,61 \pm 0,03$ MPa at 44ºC. We do not know why there is such a great difference (a factor 26 to 40) between the elastic modulus of DSPC in the gel phase respect to the other phospholipids.

The main phase transition that we report for DMPC is 25ºC, which is well related to the temperatures found in the literature which report 23ºC - 24ºC. For the gel-to-fluid transition of DPPC and DSPC we address 37ºC and 44ºC respectively. These values present an undershoot respect to the values found in the literature which show a phase transition of around 41ºC and 55ºC respectively. This inaccuracy in our temperature readings might be the result of energy loss from the cell due to evaporating water at temperatures above 40ºC. As the water level in the cell drops at increasing temperature, the system had to be refilled with water at ambient temperature, which probably induced an error in the readings. Despite these differences, the change in the elastic modulus makes us think that there are phase transitions and hence bilayers are formed.

Future works will be focused in working with loading forces in the range of piconewtons, as this is the standard range of applied forces to membranes found in the literature. The behavior of the membrane is rather complex as various observables, such as the threshold force before membrane rupture or the Young's modulus depend on several other conditions, such as the indentation velocity, the influence of the substrate in the measured stiffness, the depth of deformation, the geometry of the AFM tip, etc. Hence, the experiments have to focus on determining the relation of these quantities aiming to obtain more reproducible results. Annealing of the membranes might be of use in order to get samples with constant heights. Finally, it could be suitable to focus on studying DMPC since its main transition temperature is similar to room temperature, thus it avoids the inaccuracies due to loss of energy in the cell. For the case of DPPC and DSPC,

improvements on the cell setup must be made in order to improve the precision of the temperature measurements. For instance, to prevent water molecules to escape from the system a silicon lid covering the cell should be used.

Bibliography

[1] Gustafson, I.; *"Phospholipid membranes in biosensor applications"*, Swedish Defense Research Agency, Umeå University, Sweden, 2003.

[2] Rawicz, W., Olbrich, K. C., Mcintosh, T., Needham, D., Evans, E.; *"Effect of chain length and unsaturation on elasticity of lipid bilayers"*, Biophysical Journal **79**, 328-339, 2000.

[3] García-Manyes, S., Redondo-Morata, L., Oncins, G., Sanz, F., *"Nanomechanics of Lipid Bilayers: Heads or Tail?"*, Journal of the American Chemical Society **132**, 12874-12886, 2010.

[4] Dufrêne, Y. F., Boland, T., Schneider, J. W., Barger, W. R., Lee, G. U.; *"Characterization of the physical properties of model biomembranes at the nanometer scale with the atomic force microscope"*, Faraday Discuss, **79-94**, discussion 137-157, 1998.

[5] Smith, H. L., Jablin, M. S., Vidyasagar, A., Saiz, J., Watkins E., Toomey, R., Hurd, A. J., Majewsky, J. "*Model lipid membranes on a tunable polymer cushion",* Physical Review Letters **102**, 228102, 2009.

[6] Mey, I., Stephan, M., Schmitt, E. K., Müller, M. M., Amar, M. B., Steinem, C., Janshoff, A.; *"Local Membrane Mechanics of Pore-Spanning Bilayers"*, Journal of the American Chemical Society **131**, 7031-7039, 2009.

[7] Image by M. Ruiz, 2007.

[8] Singer, S. J., Nicolson, G. L.; "*The fluid mosaic model of the structure of cell membranes*", Science **175**, 720-731, 1972.

[9] Escrivá, P. V, Wedegaertner, P. B., Goñi, F. M., Vögler, O.; "*Lipid-protein interactions in GPCR-associated signaling*", Biochimica et Biophysica Acta **1768**, 836-852, 2007.

[10] Funari, S. S., Prades, J., Escribá, P. V., Barceló, F.; "*Farnesol and geranylgeraniol modulate the structural properties of phosphatidylethanolamine model membranes*", Molecular Membrane Biology **22**, 303-311, 2005.

[11] Barceló, F., Prades, J., Encinar, J. A., Funari, S. S., Vögler, O., Gonzalez-Ros, J. M., Escribá, P. V.; "*Interaction of the C-terminal region of the G{gamma} protein with model membranes*". Biophysics Journal **93**, 2530-2541, 2007.

[12] ©Image from Sinnauer Associates Inc., 2011.

[13] Hamley, I. W.; "*Introduction to Soft Matter: Synthetic and Biological Self-Assembling Materials* ", Wiley, New York, 2007.

[14] Jani, A. M., Zhou, J., Nussio, M. R., Losic, D., Shapter, J. G., Voelcker, N. H.; "*Pore spanning lipid bilayers on silanised nanoporus alumina membranes*", Proceedings of SPIE **7267**, 1-10, 2008.

[15] Tenchov, B., Koynova, R., Rapp, G.; "*New ordered metastable phases between the gel and subgel phases in hydrated phospholipids*", Biophysical Journal **80**, 1873-1890, 2001.

[16] Konyova, R., Caffrey, M.; "*Phases and phase transitions of phosphatidylcholines*", Biochimica et Biophysica Acta **1376**, 91-145, 1998.

[17] Meyer, H. W., Semmler, K., Rettig, W., Pohle, W., Ulrich, A. S., Grage, S., Selle, C., Quinn, P. J.; "*Hydration of DMPC and DPPC at 4^oC produces a novel subgel phase with convex-concave bilayer curvature*", Chemistry and Physics of Lipids **105**, 149-166, 2000.

[18] Retamal, M. J., Cisternas, M. A., Gutierrez-Maldonado, S. E., Perez-Acle, T., Seifert, B., Busch, M., Huber, P., Volkmann, U. G.; "*Towards biosilicon*

membrane interfaces: Formation of an ultra-thin self-hydrated membrane composed of dimalmitoylphosphatidylcholine (DPPC) and chitosan deposited in high vacumm from gas-phase", The Journal of Chemical Physics **141**, 10, 104201, 2014.

[19] Ruocco, M. J., Shipley, G. G.; "*Characterization of the subtransition of hydrated dipalmitoylphosphatidylcholine bilayers. X ray diffraction study*", Biochimica et Biophysica Acta **684**, 59-66, 1982.

[20] Nagle, J. F., Wilkinson, D. A.; "*Dilatometric studies of the subtransition in dipalmitoylphosphatidylcholine*", Biochemistry **21**, 3817-3821, 1982.

[21] Schlame, M. Casals, C., Rüstow, B., Rabe, H., Kunze, D.; "*Molecular species of phosphatidylcholine and phosphatidylglycerol in rat lung surfactant and different pools of pneumocytes type II*", Biochemical Journal **253**, 209-215, 1988.

[22] Avanti® Polar Lipids.

[23] Nagle, J. F., Wilkinson, D. A.; "*Lecithin bilayers. Density measurement and molecular interactions*", Biophysics Journal **90**, 2796-2807, 2008.

[24] Biltonen, R. L., Lichtenberg, D.; "*The use of differential scanning calorimetry as a tool to characterize liposome preparation*", Chemistry and Physics of Lipids **64**, 129-142, 1993.

[25] Kucerka, N., Nie, M. Katsaras, J.; "*Fluid phase lipid areas and bilayer thicknesses of commonly used phosphatidylcholines as a function of temperature*", Biochimica et Biophysica Acta **1808**, 2761-2771, 2011.

[26] Tompkins, H. G., Irene, E. A.; "*Handbook of ellipsometry*", Springer, 2005.

[27] Compendium, "*Principles of nulling and imaging ellipsometry*", Accurion, 2013.

[28] Azzam, R., Bashara, N.; "*Ellipsometry and polarized light*", North Holland, Second Edition, 1987.

[29] Drude, P.; "*The theory of optics* ", Dover Publications Inc., 1959.

[30] McCrackin, F. L., Passaglia, E., Stromberg, R. R. and Steinberg, H. L., "*Measurement of the thickness and refractive index of very thin films and the optical properties of surfaces by ellipsometry*", Journal of Research of the National Bureau of Standards: Physics and Chemistry, 67A, p. 363 - 377, 1963.

[31] Binning, G; Rohrer, H., Gerber, Ch., Weibel, E.; "*Surface studies by Scanning Tunneling Microscopy*", Physical Review Letters **49**, 57-60, 1982.

[32] Binning, G., Quate, C. F.; Gerber, Ch.; "*Atomic Force Microscope*", Physical Review Letters **56**, 930-933, 1986.

[33] Nanowizard® 3, "*User Manual*", JPK Instruments, 2012.

[34] Image taken from Nanophys KTH webpage.

[35] Morris, V. J., Kirby, A. R., Gunning, A. P.; "*Atomic Force Microsopy for Biologists*", Imperial College Press, Second Edition, London, 2010.

[36] Dufrene, Y. F., Boland, T., Schneider, J. W., Barger, W. R., Lee, G. U.; "*Characterization of the physical properties of model biomembranes at the nanometer scale with the atomic force microscope*", Faraday Discussions

[37] Dufrene, Y. F., Barger, W. R., Green, J. B. D., Lee, G. U., "*Nanometer-scale surface properties of mixed phospholipids monolayers and bilayers*", Langmuir **13**, 4779-4784, 1997.

[38] Braga, P. C., Ricci, D.; "*Atomic Force Microscopy: Biomedical methods and applications*", Hamana Press Inc., Totowa, 2004.

[39] Kasas, S., Thompson, N. H., Smith, B. L., Hansma, P. K., Miklossy, J., Hansma, H. G.; "*Biological application of the AFM: From single molecules*

to organs", International Journal of Imaging Systems and Technology **8**, 1-152, 2005.

[40] Radmacher, M., Cleveland, J. P., Fritz, M., Hansma, H. G., Hansma, P. K.; "*Mapping interaction forces with the atomic force microscope*", Biophysical Journal **66**, 2159-2165, 1994.

[41] Chopinet, L., Formosa, C., Rols, M. P., Duval, R. E., Dague E.; "*Imaging living cells surface and quantifying its properties at high resolution using AFM in QITM mode*", Micron **48**, 26-33, 2013.

[42] Technical Note, "*QI mode - Quantitative imaging with the Nanowizard® 3 AFM*", JPK Instruments, 2012.

[43] Butt, H. J., Capella, B., Kappl, M.; "*Force measurements with the atomic force microscope: Technique, interpretation and applications*", Surface Science Reports **59**, 1-152, 2005.

[44] Hertz, H.; "*Über die Berührung fester elasticher Körper*", Journal für die reine und angewandte Mathematik **92**, 156-171, 1881.

[45] Hutter, J. L., Bechhoefer, J.; "*Calibraition of atomic-force microscope tips*", Review of Scientific Instruments **64**, 1868-1873, 1993.

[46] Sader, J. E., Chon, J. W. M., Mulvaney, P.; "*Calibration of rectangular atomic force microscope cantilevers*", Review of Scientific Instruments **70**, 3967-3969, 1999.

[47] Tidswell, M., Ocko, B. M., Pershan, P. S., Wasserman, S. R., Whitesides, G. M., Axe, J. D.; "*X-ray specular reflection studies of silicon coated by organic monolayers (alkylsiloxanes)*", Physical Review B **41**, 1111-1128, 1990.

[48] Catalán, R. "*Fabricación de capas de silicio poroso sobre sustratos de silicio para estudios elipsométricos de muy alta resolución en biomembranas*", Tesis de Licenciatura, 2015.

[49] Franz, V., Loi, S., Müller, H., Bamberg, E., Butt, H. J.; "*Tip penetration through lipid bilayers in atomic force microscopy*", Colloids and Surfaces B: Biointerfaces **23**, 191-200, 2002.

[50] Zhou, J., Liang, D., Contera, S.; "*Effect of intra-membrane C_{60} fullerenes on the modulus of elasticity and mechanical resistance of gel and fluid lipid bilayers*", Nanoscale, **7**(40), 17102-17108, 2015.

[51] Picas, L., Rico, F., Scheuring, S.; "*Direct measurement of the mechanical properties of lipid phases in supported bilayers*", Biophysical Journal **102**, L01-L03, 2012.